Research in Computational Electromagnetics and its Applications in Wireless Communications, Imaging, and Rough Surface Scatterings

Haogang Wang

Department of Information Science and Electronic Engineering

Zhejiang University

Three Steps of the Development of CEM

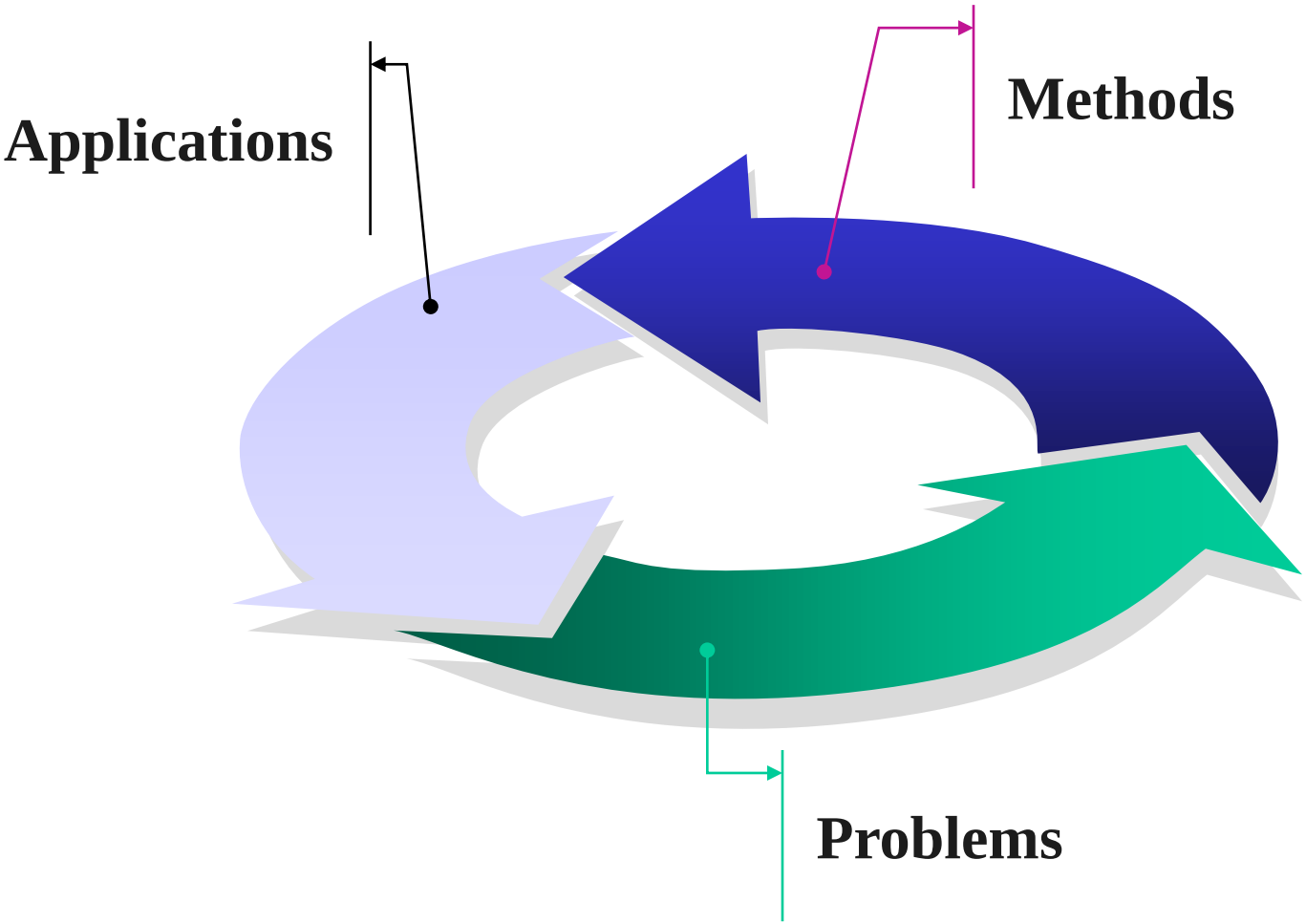

Contents

1. Numerical Algorithms;
   a) A Brief Review of the MultiLevel Green's Function Interpolation Method(MLGFIM);
   b) A Quasi-3D MLGFIM and its applications in multilayered arrays;
   c) QR Pre-ranked MLUV and its applications in rough surface scatterings.
2. Channel Mechanism Simulations and Analyses in Wireless Communications ;
   a) Rigorous Numerical Model of MIMO Wireless Communication Channel;
   b) Orbital Angular Momentum Study.
3. Superlens Imagings.

1. Numerical Algorithms

a) A Brief Review of the MultiLevel Green's Function Interpolation Method(MLGFIM)

MLGFIM: A fast three dimensional electromagnetic solver developed at City University of Hong Kong in 2003.

H. G. Wang, C. H. Chan, and L. Tsang, "A new multilevel Green's function interpolation method for large scale low frequency EM simulations," *IEEE Trans. Comput.-Aided Des. Integr. Circuits Syst.*, vol. 24, no. 9, pp. 1427–1443, Sep. 2005.

H. G. Wang and C. H. Chan, "The implementation of multilevel Green's function interpolation method for full-wave electromagnetic problems," *IEEE Trans. Antennas Propag.*, vol. 55, no. 5, pp. 1348-1358, May 2007.

Basic idea: inherit the tree-structure of MultiLevel Fast Multipole Algorithm (MLFMA), while employing a multilevel

Methods	Tree- Structure	Approx. Green's function	Available Range
MLGFIM	Yes	Interpolation	Free space, complex medium, low frequency and high frequency
MLFMA	Yes	Plane wave expansion	Free space, nonhomogeneous plane wave for mutlilayered, high frequency

1. Numerical Algorithms

a) A Brief Review of the MultiLevel Green's Function Interpolation Method(MLGFIM)

Integral equation:

$$\int_S \mathrm{d}S' G(\boldsymbol{r}, \boldsymbol{r}')\rho(\boldsymbol{r}') = 4\pi\varepsilon\phi(\boldsymbol{r})$$

The integral can be discretized into a matrix equation.

$$\overline{\overline{A}}\,\overline{x} = \overline{F}$$

where

$$A_{ij} = \begin{cases} G(\boldsymbol{r}_i, \boldsymbol{r}_j), & i \neq j \\ \int_{S_i} \mathrm{d}S \frac{1}{S_i} \int_{S_j} \mathrm{d}S' \frac{1}{S_j} G(\boldsymbol{r}, \boldsymbol{r}'), & i = j \end{cases}$$

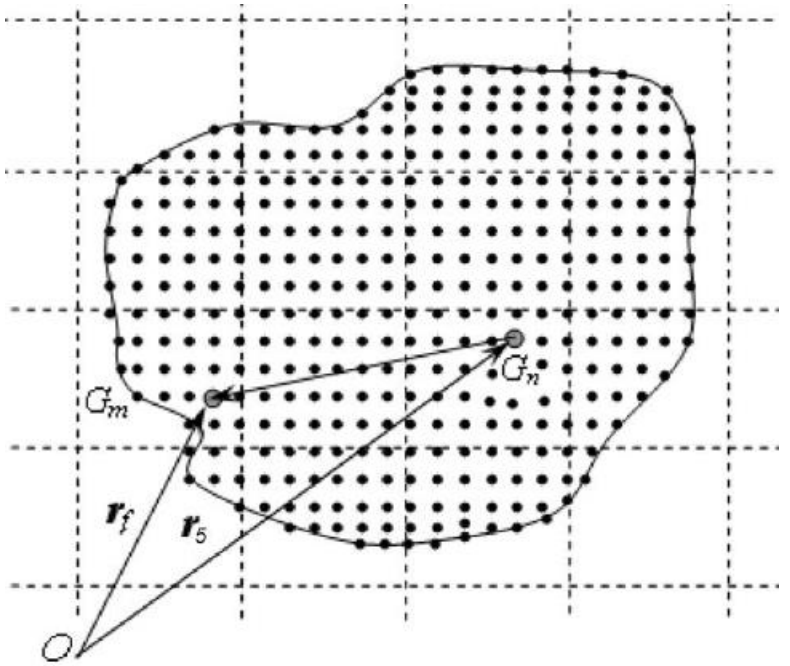

Matrix $\bar{\bar{A}}$ can be decomposed into a lot of submatrices, e. g., submatrix $\bar{\bar{A}}_{mn}$.

Here Amn describes the interactions between group Gm and group Gn.

The complexity of calculating Amn is $O(N_m * N_n)$, where N_m and N_n is the numbers of unknowns in G_m and G_n, respectively.

Question. Can we calculate $\bar{\bar{A}}_{mn}$ more fast?

1. Numerical Algorithms

a) A Brief Review of the MultiLevel Green's Function Interpolation Method(MLGFIM)

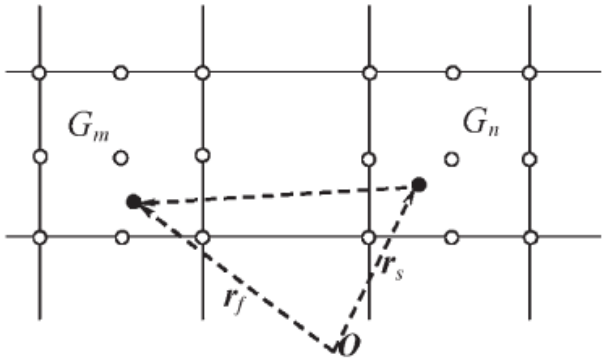

Basic idea of Green's Function Interpolations: The Green's function between the two black dots can be interpolated using the Green's functions between the white circles of group Gm and those of group Gn

$$SA_{ij} = \sum_{p=1}^{K}\sum_{q=1}^{K} \omega_{m,p}(\boldsymbol{r_i})\omega_{n,q}(\boldsymbol{r_j})G\left(\boldsymbol{r}_{G_m,p}, \boldsymbol{r}_{G_n,q}\right) \qquad SA_{ij} = \overline{\omega}_{m,i}\overline{\overline{G}}_{mn}\overline{\omega}_{n,j}$$

$$\overline{\overline{A}}_{mn} = \begin{bmatrix} \overline{\omega}_{m,1}^{\mathrm{T}} \\ \overline{\omega}_{m,2}^{\mathrm{T}} \\ \vdots \\ \overline{\omega}_{m,M_m}^{\mathrm{T}} \end{bmatrix} \overline{\overline{G}}_{mn} \left[\overline{\omega}_{n,1}, \quad \overline{\omega}_{n,2}, \ldots, \overline{\omega}_{n,M_n}\right]$$

$$= \overline{\overline{W}}_m \overline{\overline{G}}_{mn} \overline{\overline{W}}_n^{\mathrm{T}}$$

The numbers of interpolation points in a group is *K*. The complexity for calculating using the R. H. S. is $O(N_m*K+K*K+K*N_n)$.

$K << N_m$ or N_n, thus $N_m*K+K*K+K*N_n << N_m*N_n$.

Calculation for the R. H. S. is more efficient than for the L. H. S.

Some Applications

1. Capacitance extractions (low frequency problems);

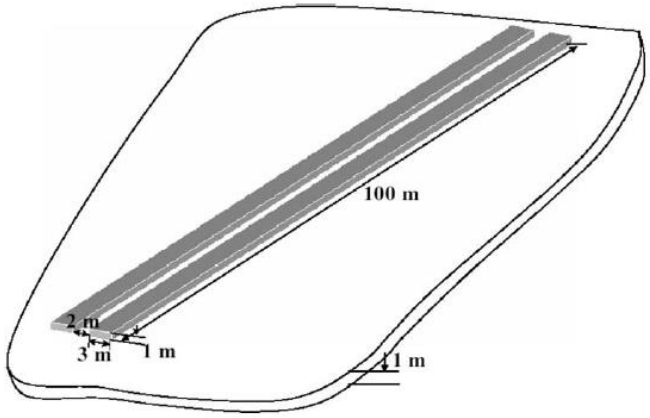

Two parallel conductors on a slab with a relative permittivity of 2.

CAPACITANCES OF THE COUPLED INTERCONNECT. UNITS ARE IN FARADS PER METER

Capacitance	Our Results	Reference [27]	Reference [28]	Reference [29]
C11	0.9498×10^{-10}	0.9165×10^{-10}	0.9017×10^{-10}	0.9224×10^{-10}
C12	-0.8224×10^{-11}	-0.8220×10^{-11}	-0.8059×10^{-11}	-0.8504×10^{-11}
C21	-0.8224×10^{-11}	-0.8220×10^{-11}	-0.8059×10^{-11}	-0.8504×10^{-11}
C22	0.9498×10^{-10}	0.9165×10^{-10}	0.9017×10^{-10}	0.9224×10^{-10}

H. G. Wang, C. H. Chan, and L. Tsang, "A new multilevel Green's function interpolation method for large scale low frequency EM simulations," *IEEE Trans. Comput.-Aided Des. Integr. Circuits Syst.*, vol. 24, no. 9, pp. 1427–1443, Sep. 2005.

1. Numerical Algorithms

a) A Brief Review of the MultiLevel Green's Function Interpolation Method(MLGFIM)

2. Inductance extractions (low frequency problems);

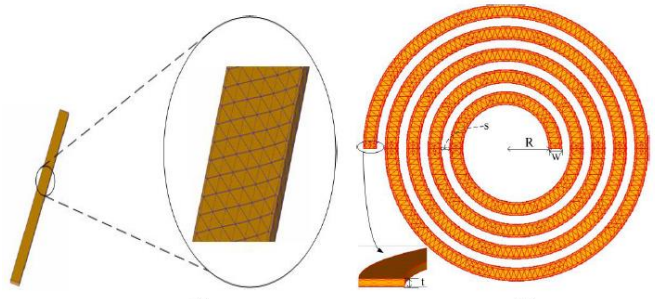

(a) A rectangular straight line with 5 microns by 30 microns by 1000 microns. (b) A 4.5 turns inductor. $w = 30$ microns, $t = 3$ microns, $s = 20$ microns, and $R = 100$ microns.

Inductances of the straight line and spiral inductors.

Examples	Frequency	Inductance (nH)		
		MLGFIM-VL	Fast Henry	Difference (%)
Straight line (in Fig. 3)	2 GHz	0.884541	0.884935	0.04
	10 GHz	0.881354	0.898938	1.95608
1.5 turns spiral inductor	13 Hz	0.981343	0.994345	1.30759
	13 GHz	0.942563	0.966121	2.43841
2.5 turns spiral inductor	6.3 Hz	2.56795	2.60564	1.44648
	6.3 GHz	2.46407	2.54221	3.07370
3.5 turns spiral inductor	4.4 Hz	5.08489	5.21537	2.50184
	4.4 GHz	4.89556	5.10688	4.13795
4.5 turns spiral inductor	2.8 Hz	8.81897	9.02001	2.22882
	2.8 GHz	8.50109	8.85870	4.03682

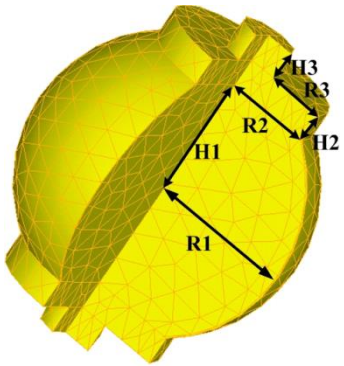

The inductances and resistances of the spiral inductors of 2.5 turns and 3.5 turns and the bump . ($f = 10$ GHz).

Examples at 10 GHz	FCSIE-MLGFIM		VLIE [2]		FastHenry [16]	
	R (Ohm)	L (nH)	R (Ohm)	L (nH)	R (Ohm)	L (nH)
2.5 turn spiral inductor	1.223	2.215	1.889	2.229	1.189	2.248
3.5 turn spiral inductor	2.106	4.4	3.296	4.420	1.965	4.487
Bump	0.0621	0.0355		0.0339		

P. Zhao and H. G. Wang, "Resistances and inductances extraction using surface integral equation with the acceleration of multilevel Green's function interpolation method," PIER 83, 43-54, 2008.

H. G. Wang, P. Zhao, "Combining Multilevel Green's Function Interpolation Method with volume loop bases for inductance extraction problems," *Progress In Electromagnetics Research*, PIER 80, 225-239, 2008.

1. Numerical Algorithms

a) A Brief Review of the MultiLevel Green's Function Interpolation Method(MLGFIM)

4. Scattering problems (high frequency problems)

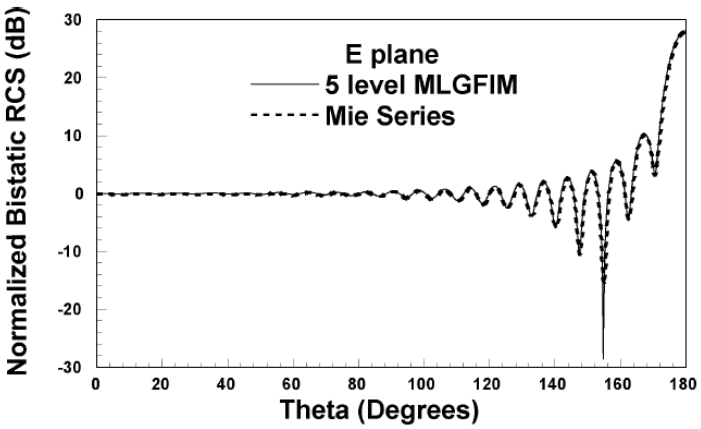

E plane RCS results of an 8 wavelength sphere.

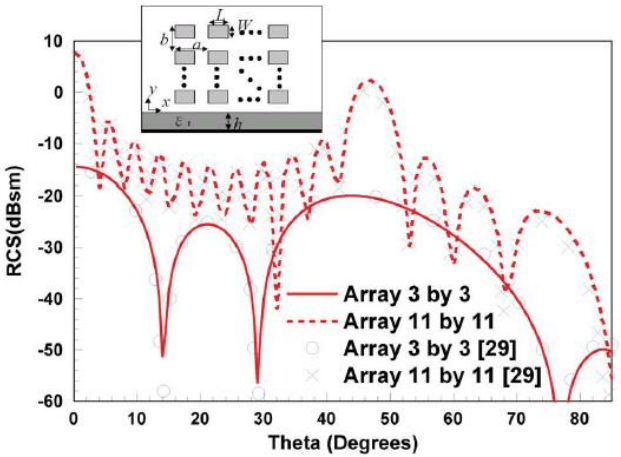

(a) $\theta - \theta$ polarized RCS of the 3-by-3 and 11-by-11 arrays. $a = b = 5.5517$ cm, $L = 3.66$ cm, $W = 2.6$ cm, $h = 0.158$ cm, $\varepsilon_r = 2.17$, $f = 3.7$ GHz, and $\varphi = 0°$.

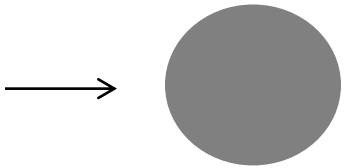

H. G. Wang and C. H. Chan, "The implementation of multilevel Green's function interpolation method for full-wave electromagnetic problems," *IEEE Trans. Antennas Propag.*, vol. 55, no. 5, pp. 1348-1358, May 2007.

1. Numerical Algorithms

a) A Brief Review of the MultiLevel Green's Function Interpolation Method(MLGFIM)

4. Scattering problems;

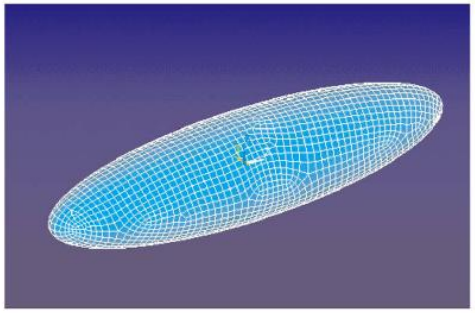

(a)

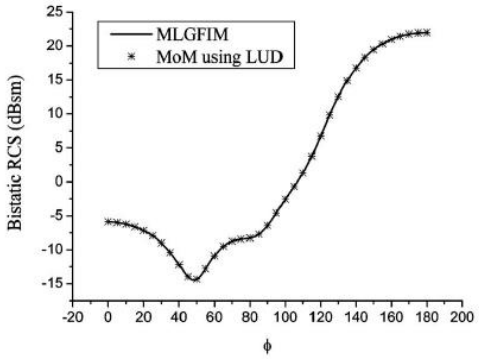

(b)

(Color online) Plane-wave scattering from a dielectric elliptical sphere: (a) geometry of elliptical sphere; (b) bistatic RCS with $\phi\phi$ polarization.

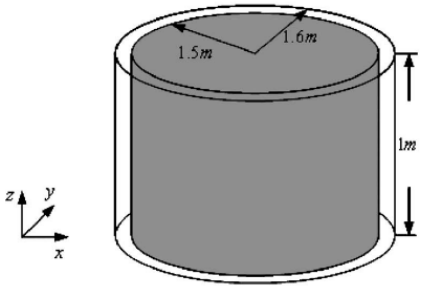

(a)

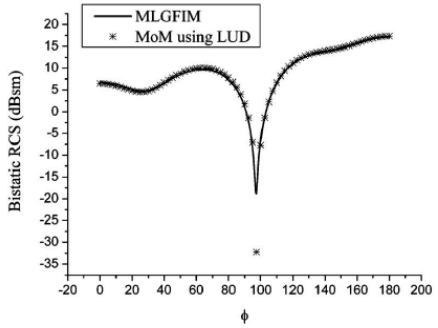

(b)

Plane-wave scattering from a PEC cylinder coated by air dielectric material: (a) geometry, (b) bistatic RCS with $\phi\phi$ polarization.

Yan Shi, Hao Gang Wang, Long Li, and Chi Hou Chan, "Multilevel Green's function interpolation method for scattering from composite metallic and dielectric objects," *J. Opt. Soc. Am.* A/Vol. 25, No. 10. pp. 2535-2548, October 2008

5. Radiation problems (high frequency problems)

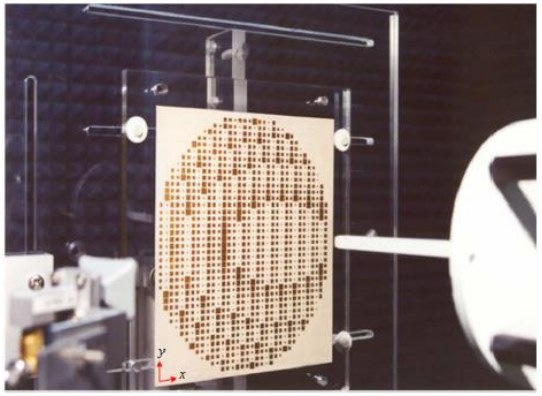

Near-field experimental setup used to measure the reflectarray.

(Freq=28 GHz. Epsilonr=2.94, Thickness=0.762 mm.)

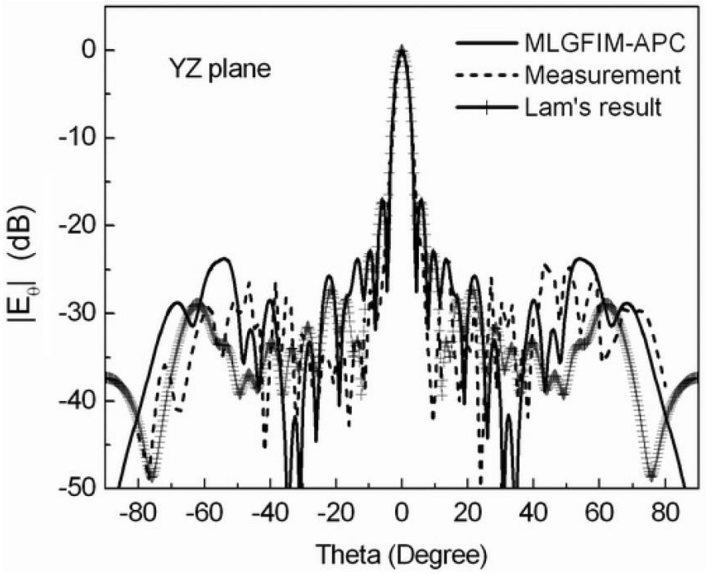

Radiation pattern of 1 117 square patch reflectarray in yz plane excited by an offset horn with TE polarization.

L. Li, H. G. Wang, C. H. Chan, "An improved multilevel Green's function interpolation method with adaptive phase compensation," *IEEE Trans. Antennas and Propag.*, Vol. 56, No. 5, pp. 1381-1393, May 2008.

1. Numerical Algorithms

b) A Quasi-3D MLGFIM and its applications in multilayered arrays

An algorithm suitable for layered structures.

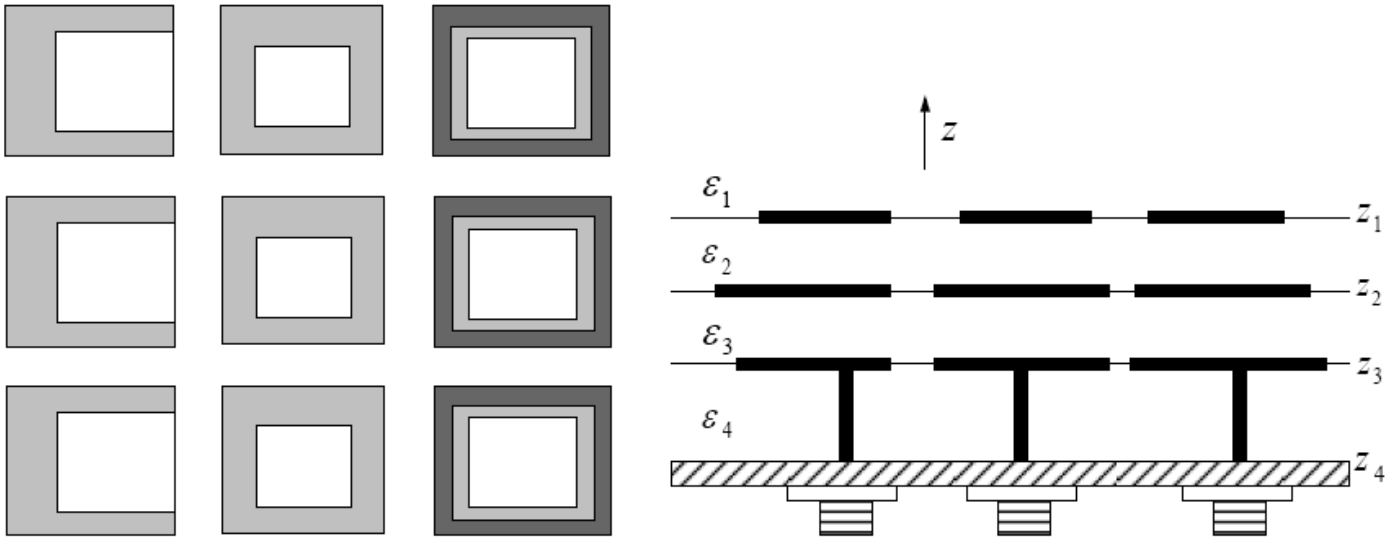

Illustration of antenna array structure in multilayered medium. (a) top view. (Only the antenna patches are shown). (b) side view.

Hao Gang Wang、 Huan Li、 Da Qing Liu、 Xin Hua Yu ， A Quasi-Three Dimensional Multi-Level Green's Function Interpolation Method for Multilayered Structures ， Electromagnetics in Advanced Applications (ICEAA), 2010 International Conference on, 20/9/2010-24/9/2010, pp 125-128, 2010/9/20.

Da Qin Liu, Huan Li, Hao Gang Wang, and Yang Du, "Multi-GPOF Method in the Calculation of the Rectangular Waveguide Layered Green's Functions," *IEEE Antennas and Wireless Propag. letters*, Vol. 9, pp. 1143-1147, 2010.

H. Li and H. G. Wang, "An improvement of the Ge-Esselle's method for the evaluation of the Green's functions in the shielded multilayered structures," PIER 88, pp. 149-161, 2008.

1. Numerical Algorithms

b) A Quasi-3D MLGFIM and its applications in multilayered arrays

Half space problem:

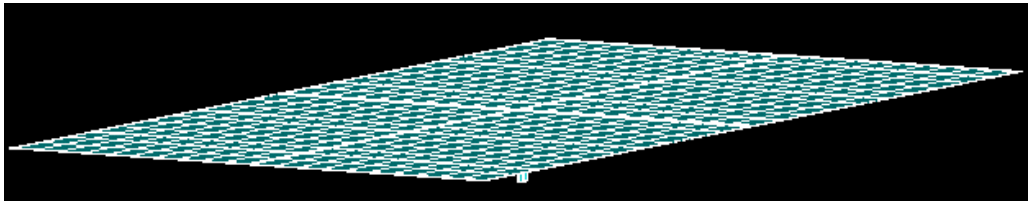

(Unit: mm)

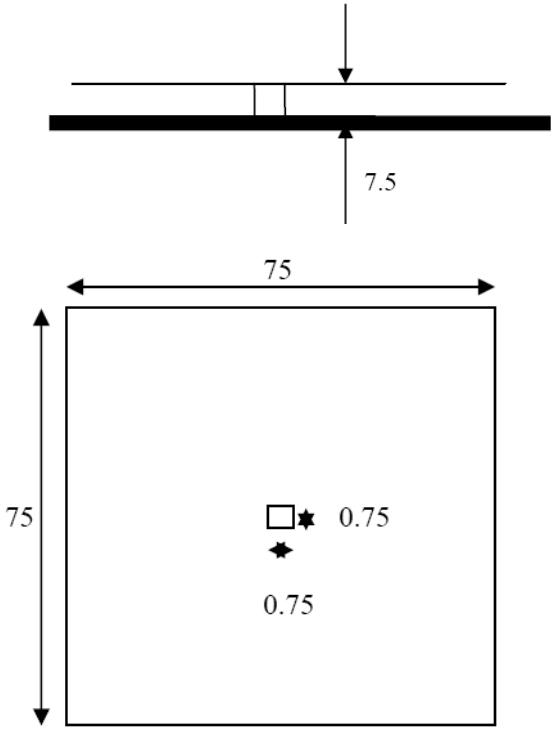

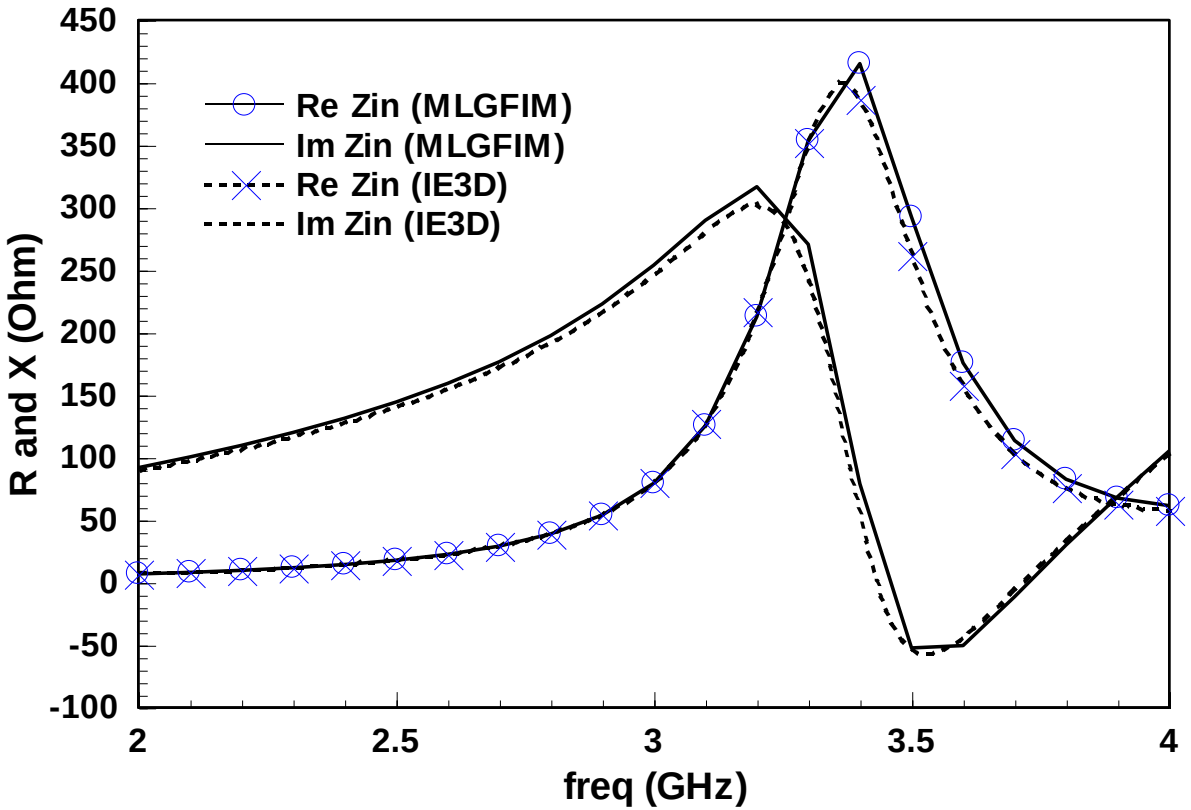

Complexity Analysis

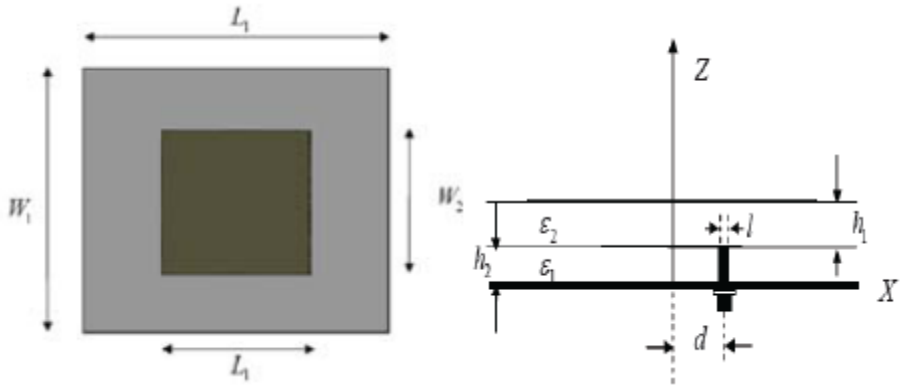

Schematic diagram of one cell of the stacked microstrip patch antenna array. $W_1 = 31.69$

$L_1 = 34.86$ $W_2 = L_2 = 16.54$ $h_1 = 3.27$ $h_2 = 3.17$ $d = 7.18$ $l = 0.94$ $\varepsilon_1 = 1.07$ $\varepsilon_2 = 10.4$. (mm)

The geometry of a 3-by-3 array.

The arrangement of the simulated arrays.

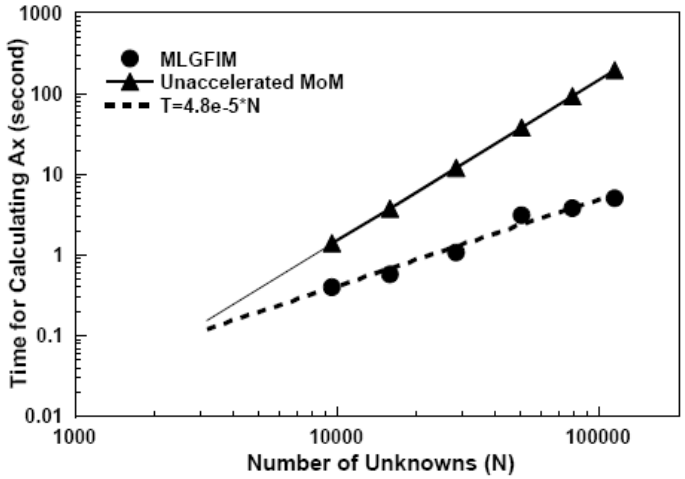

CPU time per Ax vs. number of unknowns.

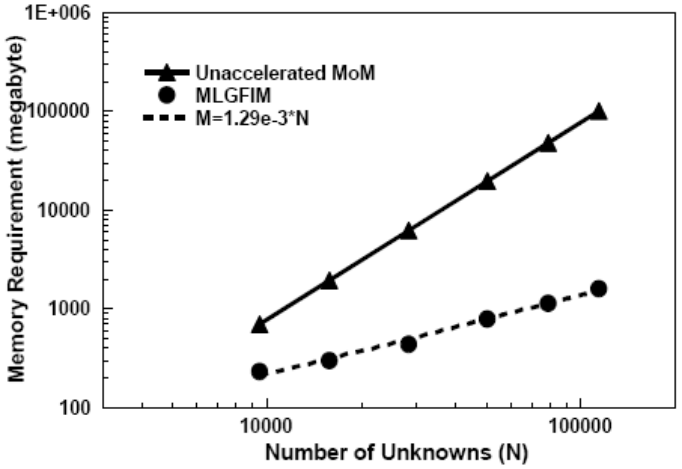

Memory requirement vs. number of unknowns.

1. NUMERICAL ALGORITHMS

C) QR PRE-RANKED MLUV AND ITS APPLICATIONS IN ROUGH SURFACE SCATTERINGS

Soil Rough surface Modeled by Exponential Correlation function

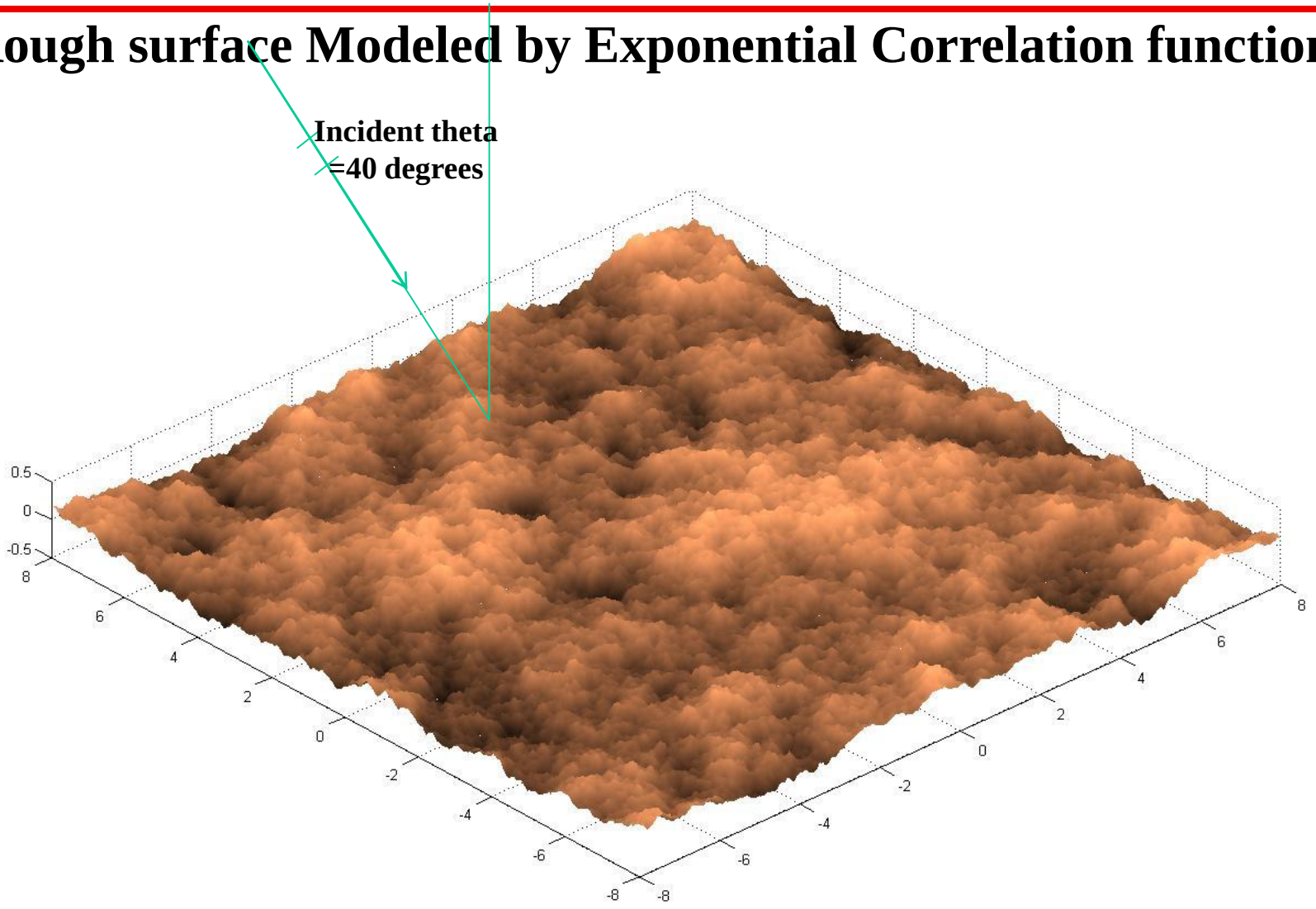

Soil rough surface after triangle meshing

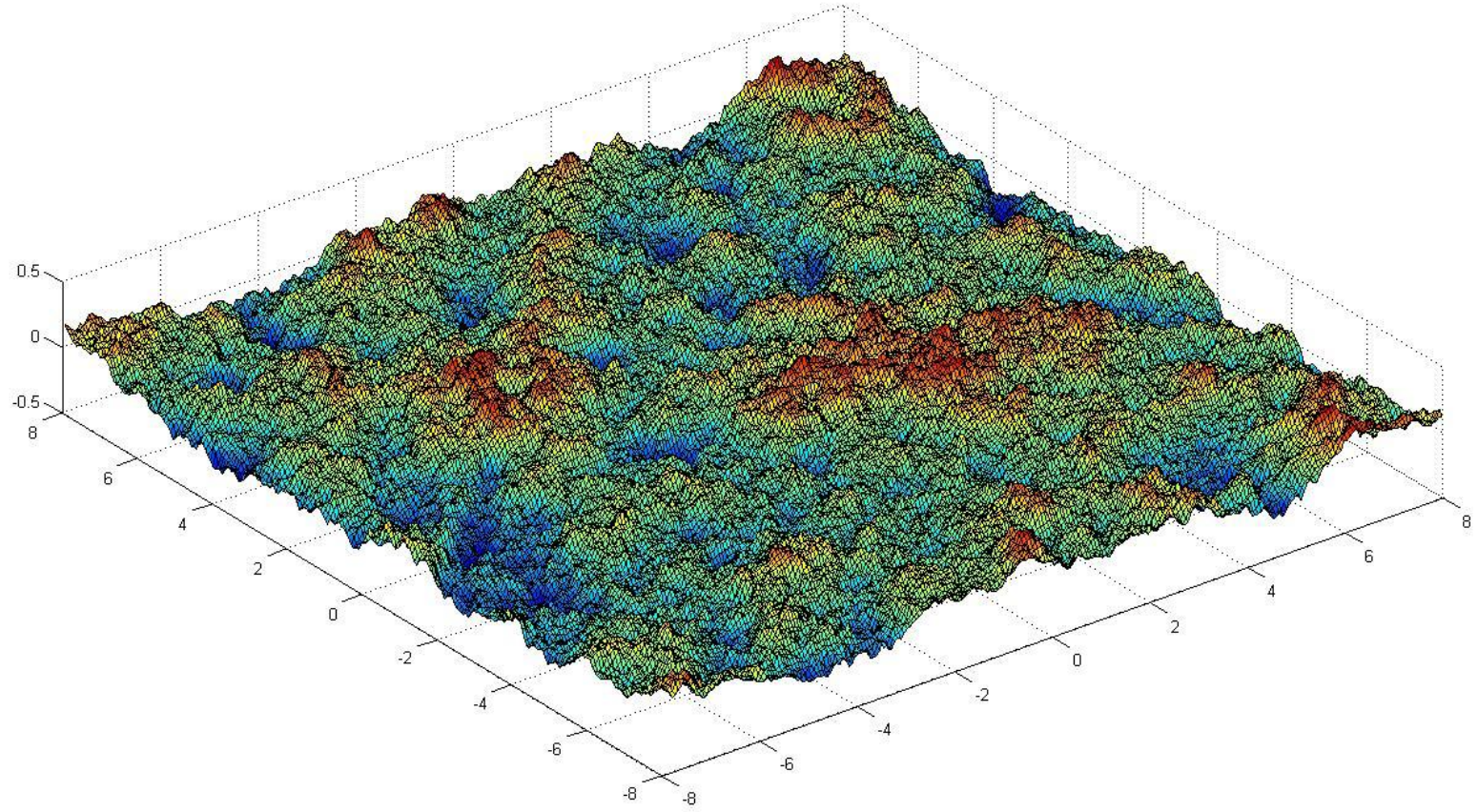

1. NUMERICAL ALGORITHMS

C) QR PRE-RANKED MLUV AND ITS APPLICATIONS IN ROUGH SURFACE SCATTERINGS

PMCHWT formulations

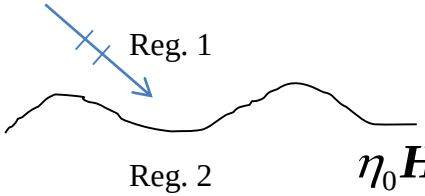

$$\boldsymbol{E}^{inc}(\boldsymbol{r})|_{\tan} = (L_1 + L_2)\boldsymbol{J}'(\boldsymbol{r})|_{\tan} - (K_1 + K_2)\boldsymbol{M}(\boldsymbol{r})|_{\tan}$$

$$\eta_0 \boldsymbol{H}^{inc}(\boldsymbol{r})|_{\tan} = (K_1 + K_2)\boldsymbol{J}'(\boldsymbol{r})|_{\tan} + (\varepsilon_{r1} L_1 + \varepsilon_{r2} L_2)\boldsymbol{M}(\boldsymbol{r})|_{\tan}$$

$$\boldsymbol{J}'(\boldsymbol{r}') = \eta_0 \boldsymbol{J}(\boldsymbol{r}')$$

$$G_i(\boldsymbol{r},\boldsymbol{r}') = \exp(ik_i R)/R$$

$$i = 1, 2$$

$$L_i = \frac{-i\omega\mu_i}{4\pi\eta_0}\int_S ds'(\bar{\bar{I}} - \frac{1}{k_i^2}\nabla\nabla')G_i(\boldsymbol{r},\boldsymbol{r}')\cdot$$

$$K_i = -\frac{1}{4\pi}\int_S ds'\nabla G_i(\boldsymbol{r},\boldsymbol{r}')\times$$

Galerkin method and RWG Bases are used. The PMCHWT can be converted to

$$\begin{bmatrix} \bar{\bar{Z}}^{LE} & -\bar{\bar{Z}}^{K} \\ \bar{\bar{Z}}^{K} & \bar{\bar{Z}}^{LM} \end{bmatrix}\begin{bmatrix} \bar{I}^{E} \\ \bar{I}^{M} \end{bmatrix} = \begin{bmatrix} \bar{\bar{Z}}^{L_1} + \bar{\bar{Z}}^{L_2} & -(\bar{\bar{Z}}^{K_1} + \bar{\bar{Z}}^{K_2}) \\ \bar{\bar{Z}}^{K_1} + \bar{\bar{Z}}^{K_2} & \varepsilon_{r1}\bar{\bar{Z}}^{L_1} + \varepsilon_{r2}\bar{\bar{Z}}^{L_2} \end{bmatrix}\begin{bmatrix} \bar{I}^{E} \\ \bar{I}^{M} \end{bmatrix} = \begin{bmatrix} \bar{V}^{E} \\ \bar{V}^{M} \end{bmatrix}$$

The entries of the impedance matrix

$$Z_{p,q}^{L_i} = \frac{-i\omega\mu_i}{4\pi\eta_0}\int_S ds\,\boldsymbol{f}_p(\boldsymbol{r})\cdot\int_S ds'[\bar{\bar{I}} - \frac{1}{k_i^2}\nabla\nabla']G_i(\boldsymbol{r},\boldsymbol{r}')\cdot\boldsymbol{f}_q(\boldsymbol{r}')$$

$$Z_{p,q}^{K_i} = -\frac{1}{4\pi}\int_{S_p} ds\boldsymbol{f}_p(\boldsymbol{r})\cdot\int_{S_q} ds'\nabla G_i(\boldsymbol{r},\boldsymbol{r}')\times\boldsymbol{f}_q(\boldsymbol{r}')$$

1. NUMERICAL ALGORITHMS
C) QR PRE-RANKED MLUV AND ITS APPLICATIONS IN ROUGH SURFACE SCATTERINGS

The subscatterers on the rough surface is multilevel divided into a lot of square groups. At each level, the interactions between two groups are just the entries of one submatrix in the impedance matrix. To fully calculate these interactions require O(m*n) complexity, where m and n are the numbers of the subscatterers in the source and field groups.

Basic idea of UV($\bar{\bar{Z}}_{mn} \approx \bar{\bar{U}}_{ms} \cdot \bar{\bar{V}}_{sn}$):

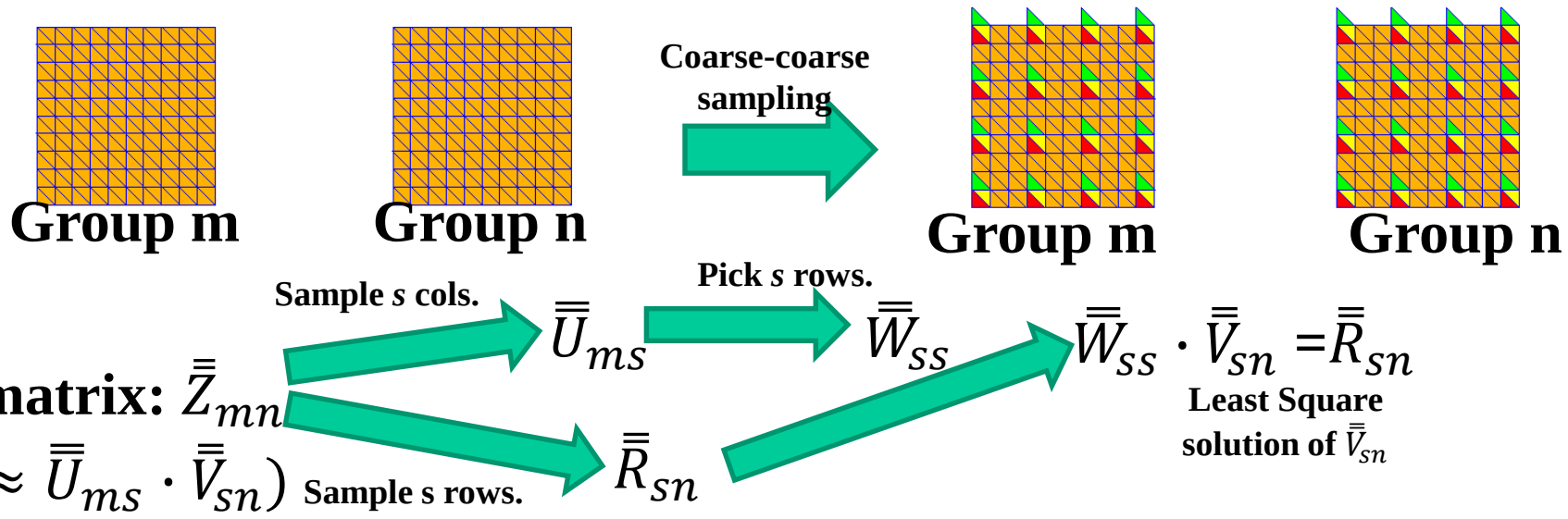

Tsang, L., Li, Q., and Xu, P. *et al.*, "Wave scattering with the UV multilevel partitioning method: 2. Three-dimensional problem of nonpenetrable surface scattering," *Radio Sci.* 39(5) RS5011 (2004).

Always, *s* is greater than *r* the numerical ranks of the interaction submatrix. This causes the deficiency of the algorithm.

1. NUMERICAL ALGORITHMS

C) QR PRE-RANKED MLUV AND ITS APPLICATIONS IN ROUGH SURFACE SCATTERINGS

Basic idea of QR: $\overline{\overline{(Z_{mn}}} \approx \bar{\bar{Q}}_{mr} \cdot \bar{\bar{R}}_{rn})$

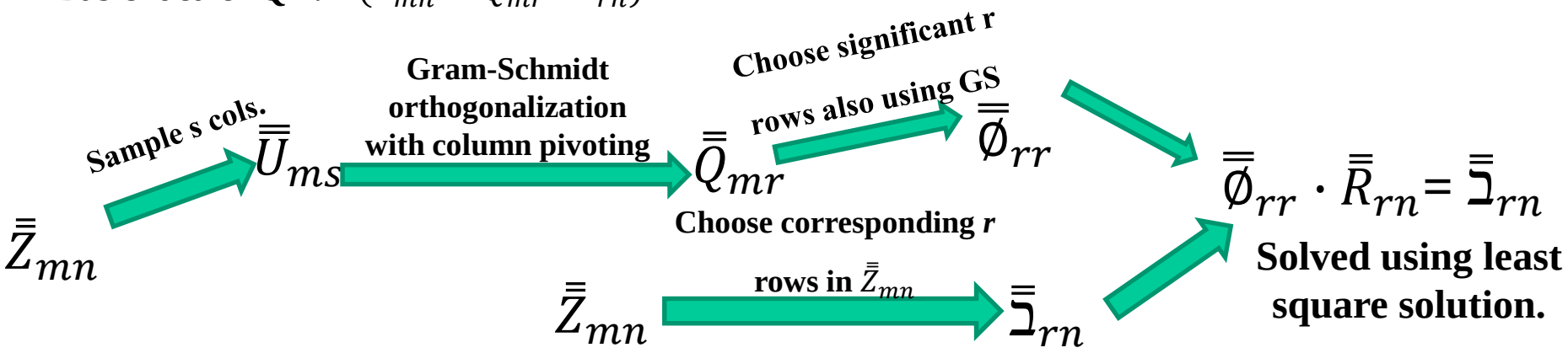

Analyses:

- The storage used in storing submatrices $\bar{\bar{Q}}_{mr}$ and $\bar{\bar{R}}_{rn}$ is less than that for $\bar{\bar{U}}_{ms}$ and $\bar{\bar{V}}_{sn}$;
- The Gram-Schmidt (QR) algorithm with a complexity of *m*s*s* should be used in QR;
- *s* is always greater than *r* the numerical rank of $\bar{\bar{Z}}_{mn}$.

Idea: combine UV with rank pre-evaluation using QR.

1. NUMERICAL ALGORITHMS

C) QR PRE-RANKED MLUV AND ITS APPLICATIONS IN ROUGH SURFACE SCATTERINGS

Flow chart of CCS MLUV and QR-Pre-Ranled MLUV

In QR-Pre-Ranked MLUV, Gram-Schmidt (QR) algorithm is only performed on $\bar{\bar{W}}_{ss}$, the sampled matrix from $\bar{\bar{Z}}_{mn}$. The complexity for this step is *s*s*s.

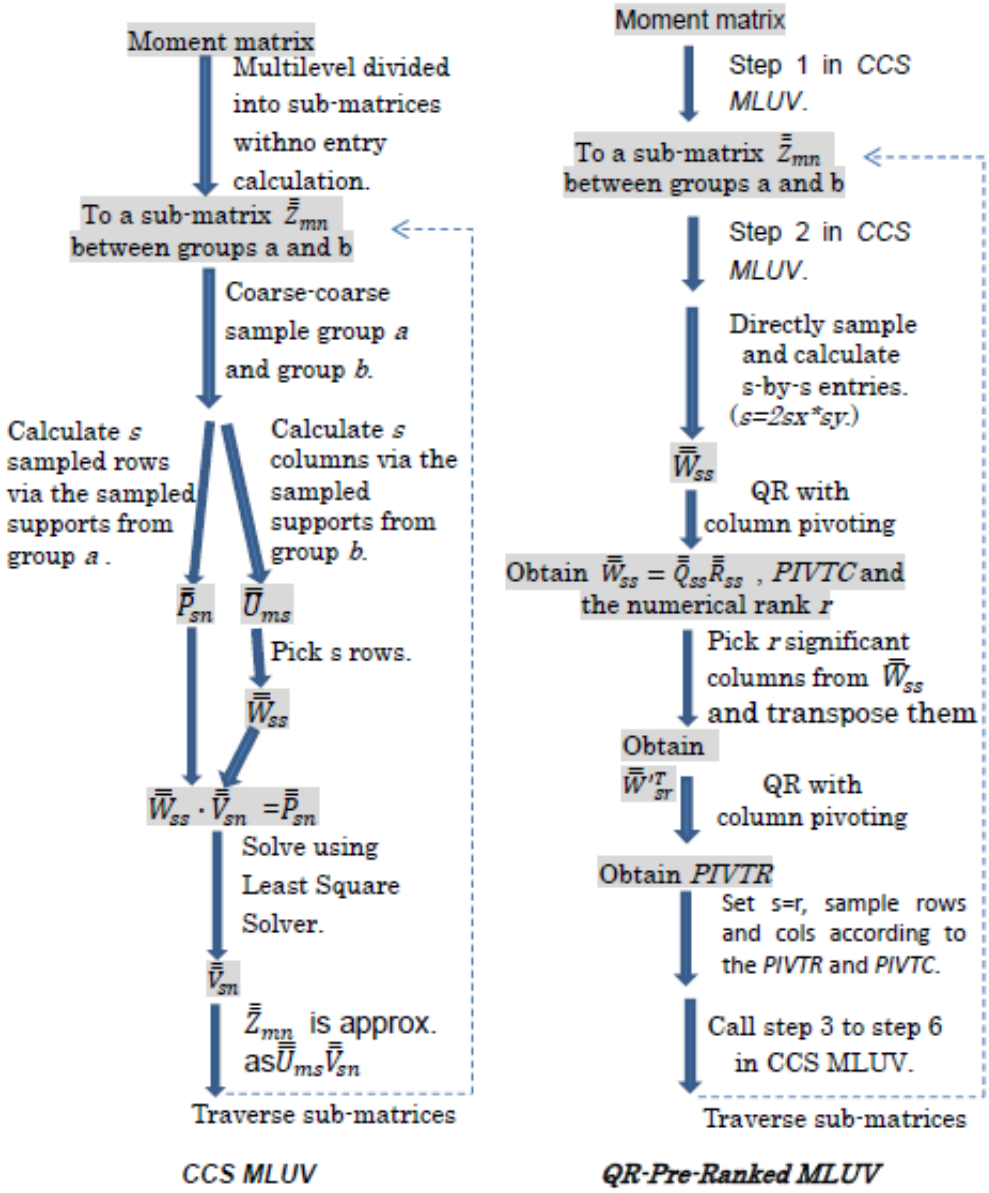

Comparisons of the Emissivity

ZJU: Data from Zhejiang University;
UW: Data from University of Washington

	ev (ZJU)	ev (UW)	eh (ZJU)	eh (UW)
rms=0.021	0.751	0.7504	0.562	0.5611
rms=0.042	0.759	0.7599	0.582	0.5797
rms=0.084	0.799	0.7762	0.604	0.6140

ev: Emissivity of V pol.;
eh: Emissivity of H pol.

cL/rms=10

EPS = 15 +3.5i

Comparison of the Incoherent Back Scattering Coefficients

	VV (UW)	VV (ZJU)	HH (UW)	HH (ZJU)
RMS=0.021 λ	-18.68	-18.35	-22.68	-22.78
RMS=0.042 λ	-14.79	-14.06	-18.37	-18.39
RMS=0.084 λ	-11.88	-11.03	-14.49	-14.56

CL/RMS = 10
Incident Angle = 40 degree
EPS = 15 +3.5i
UW : 16 by 16 square wavelength (16 points per wavelength)， 30 realizations
Wang : 16 by 16 square wavelength (16 points per wavelength), 20 realizations

1. NUMERICAL ALGORITHMS

C) QR PRE-RANKED MLUV AND ITS APPLICATIONS IN ROUGH SURFACE SCATTERINGS

Complexity

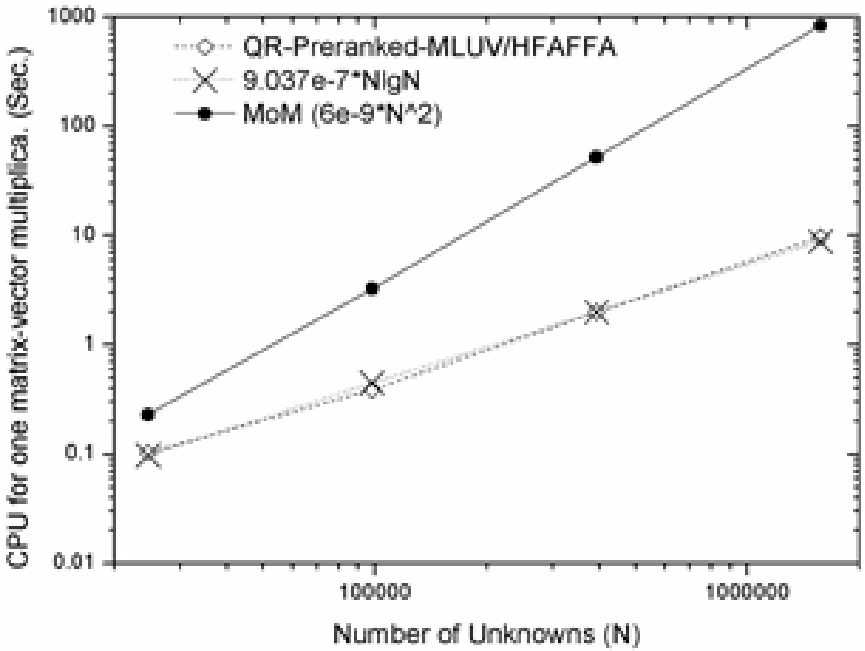

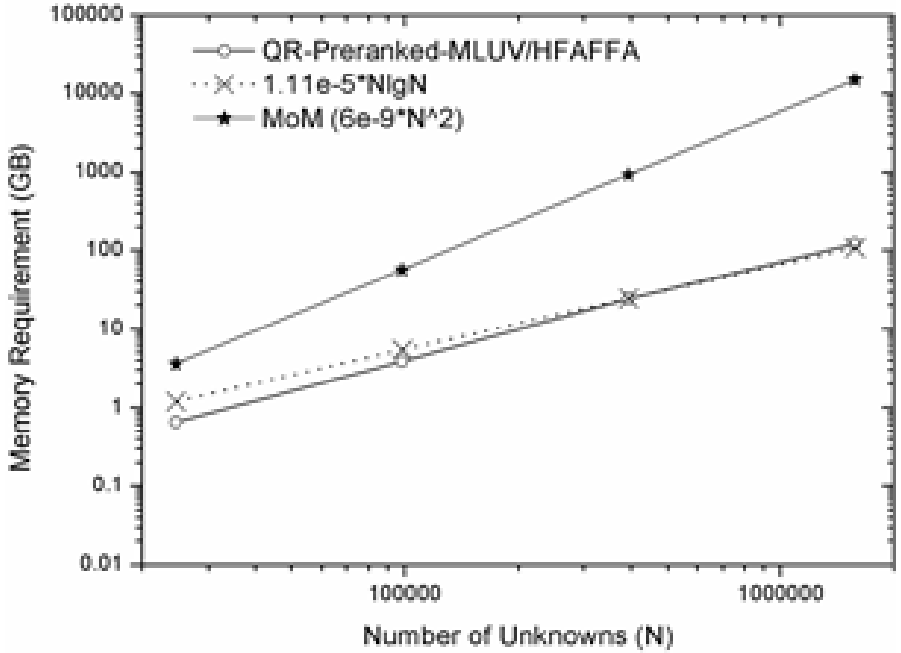

1. NUMERICAL ALGORITHMS

C) QR PRE-RANKED MLUV AND ITS APPLICATIONS IN ROUGH SURFACE SCATTERINGS

Incoherent bistatic coefficients for case cL=0.084.

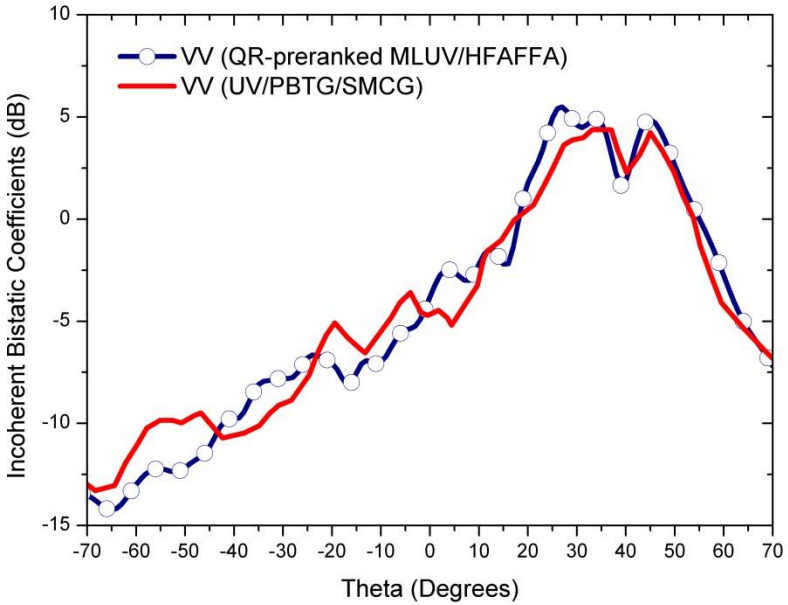

Incoherent Bistatic Coefficients for VV polarization case.

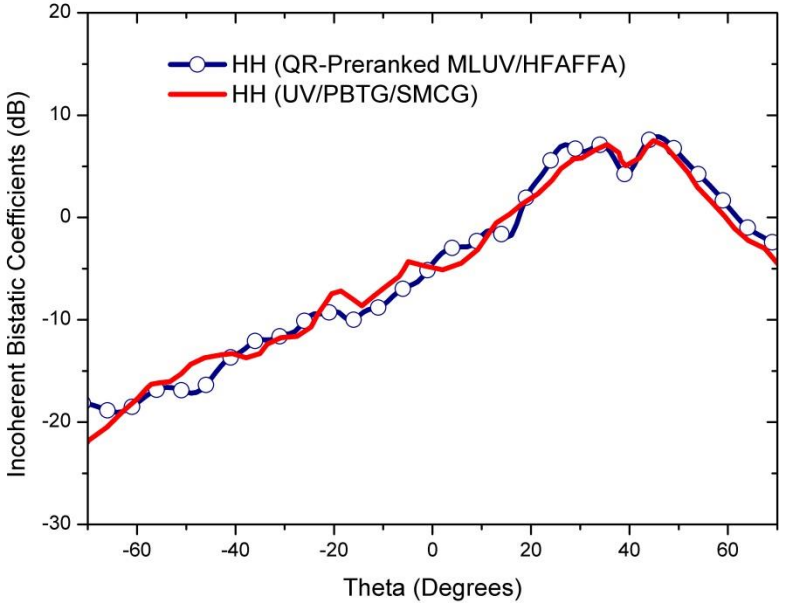

Incoherent Bistatic Coefficients for HH polarization case.

2. CHANNEL MECHANISM SIMULATIONS AND ANALYSES IN WIRELESS COMMUNICATIONS

a) Rigorous Numerical Model of MIMO Wireless Communication Channel

Numerical Model for MIMO Channels using MLGFIM

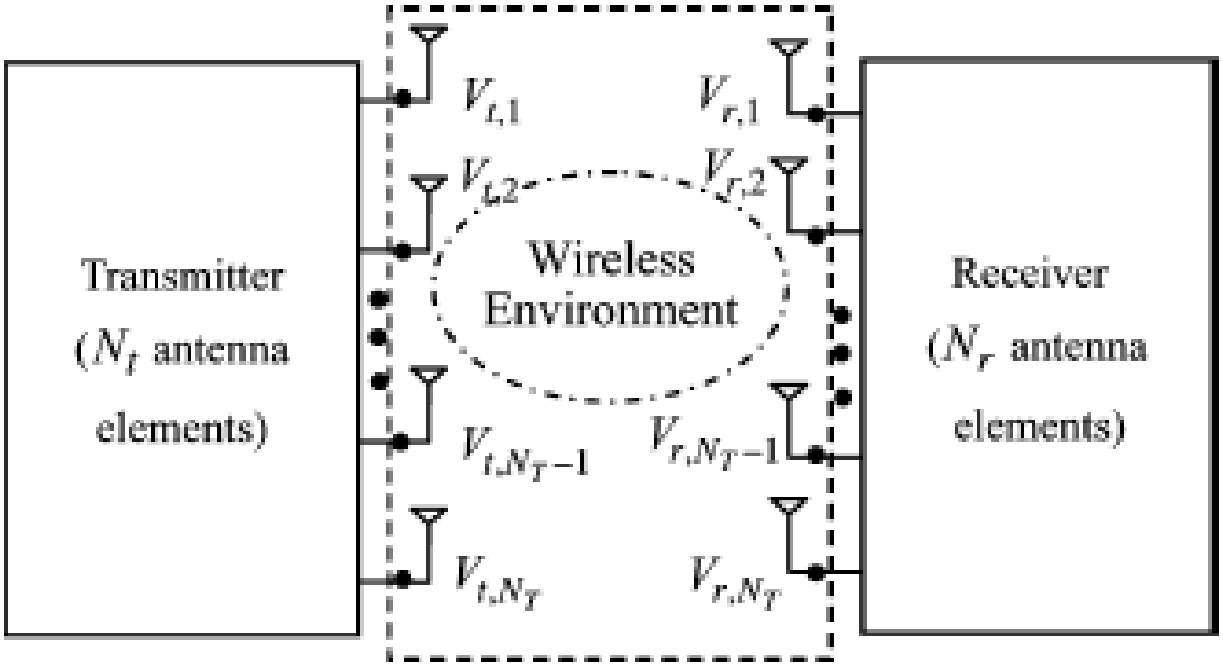

- ***H. G. Wang, L. Wang, H. Li, H. B. Song, and K. Hong, "A Novel Numerical Model for Simulating Three Dimensional MIMO Channels with Complex Antenna Arrays," IEEE Transactions on Antennas and Propagation, Vol. 57, no. 8, August, pp. 2439-2451, 2009.***
- **H.-G. Wang, L. Wang, H. Li, H.-B. Song, K. Hong, "Design and numerical analyses of an indoor 3–5 GHz UWB-MIMO array," *IET Microwaves, Antennas & Propagation*,Vol.4, pp. 1517-1524, 2010.**
- **H. B. Song, H. G. Wang, K. Hong, and L. Wang, "A Novel Source Localization Scheme Based on Unitary ESPRIT and City Electronic Maps in Urban Environments," *PIER 94,* pp. 243-262, 2009.**

Equivalent MIMO Channel

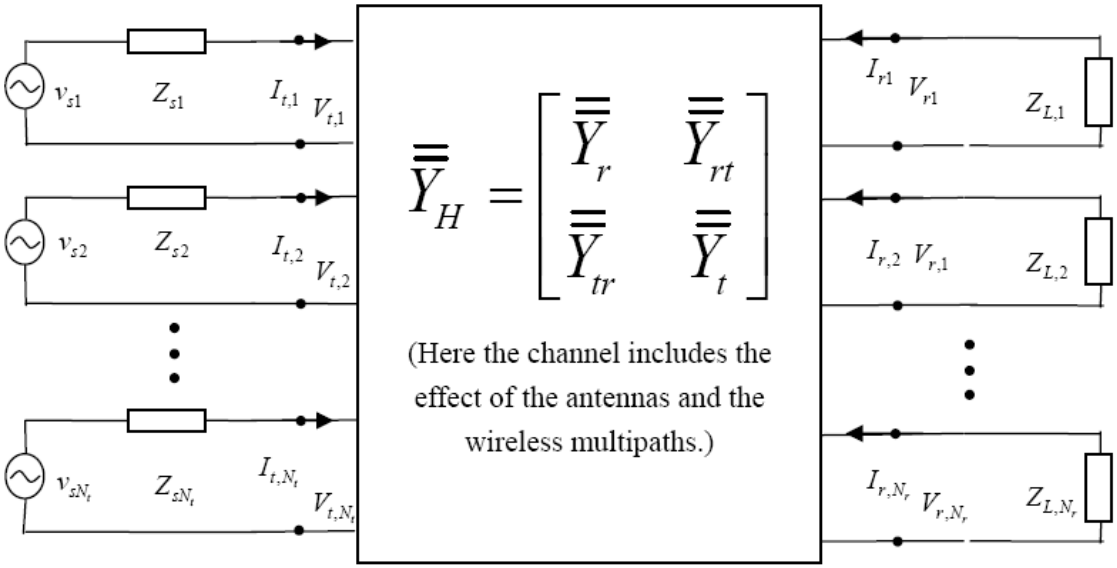

$$\bar{V}_r = -(\bar{\bar{Z}}_L^{-1} + \bar{Y}_r)^{-1} \cdot \bar{\bar{Y}}_{rt} \cdot (\bar{\bar{Z}}_s^{-1} + \bar{Y}_t)^{-1} \cdot \bar{\bar{Z}}_s^{-1} \cdot \bar{V}_s = \bar{\bar{H}} \cdot \bar{V}_s$$

Channel Matrix $\bar{\bar{H}} = -(\bar{\bar{Z}}_L^{-1} + \bar{Y}_r)^{-1} \cdot \bar{\bar{Y}}_{rt} \cdot (\bar{\bar{Z}}_s^{-1} + \bar{Y}_t)^{-1} \cdot \bar{\bar{Z}}_s^{-1}$

2. CHANNEL MECHANISM SIMULATIONS AND ANALYSES IN WIRELESS COMMUNICATIONS

a) Rigorous Numerical Model of MIMO Wireless Communication Channel

Calculation of the Channel Matrix Using MLGFIM+Ray Tarcing Method

Channel: $$\bar{\bar{H}} = -(\bar{\bar{Z}}_L^{-1} + \bar{Y}_r)^{-1} \cdot \bar{\bar{Y}}_{rt} \cdot (\bar{\bar{Z}}_s^{-1} + \bar{Y}_t)^{-1} \cdot \bar{\bar{Z}}_s^{-1}$$

Yr and Yt: Calculated using MLGFIM;

Yrt: Calculated using MLGFIM with Ray Tracing.

H. G. Wang, L. Wang, H. Li, H. B. Song, and K. Hong, "A Novel Numerical Model for Simulating Three Dimensional MIMO Channels with Complex Antenna Arrays," IEEE Transactions on Antennas and Propagation, Vol. 57, no. 8, August, pp. 2439-2451, 2009.

Examples

a) Indoor Environment:

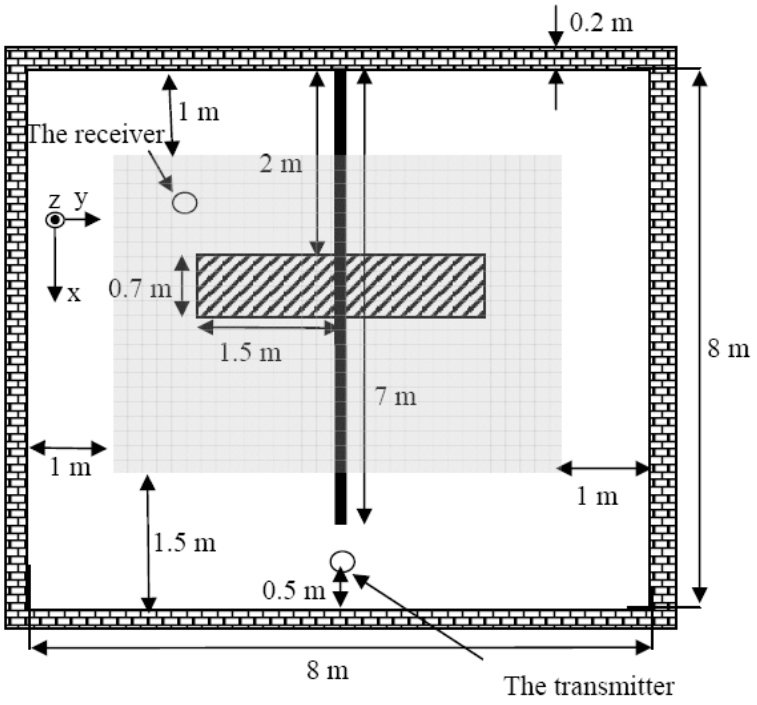

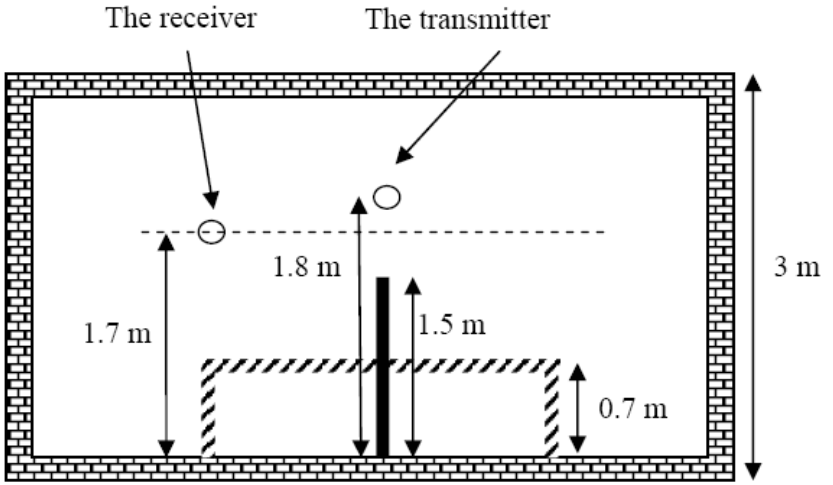

2. CHANNEL MECHANISM SIMULATIONS AND ANALYSES IN WIRELESS COMMUNICATIONS

a) Rigorous Numerical Model of MIMO Wireless Communication Channel

b) Test Arrays

Frequency: 1.969 GHz
Monopole h: 35.8 mm
Monopole radius: 1.18 mm.

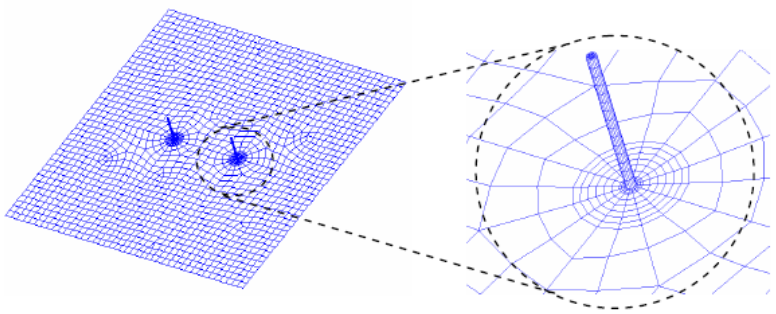

Space between Monopoles:
0.5 wavelengths

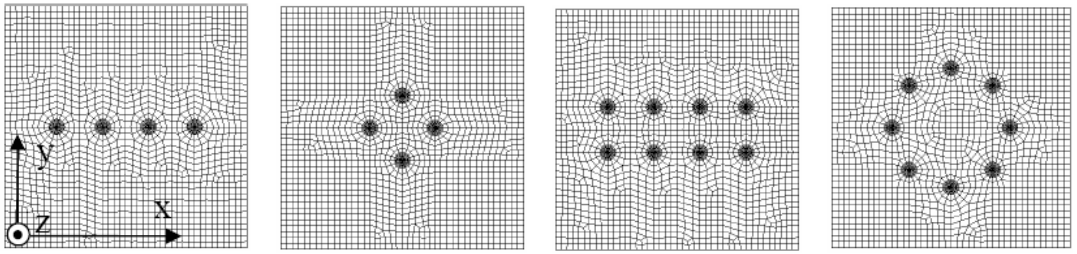

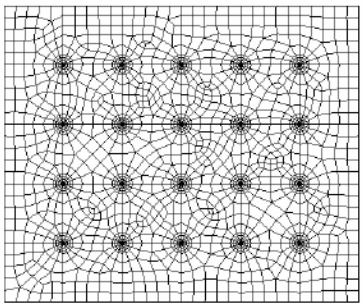

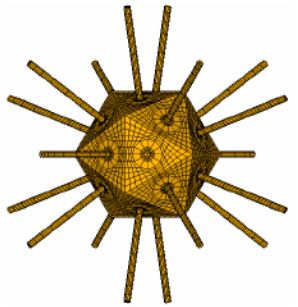

Icosahedron Array

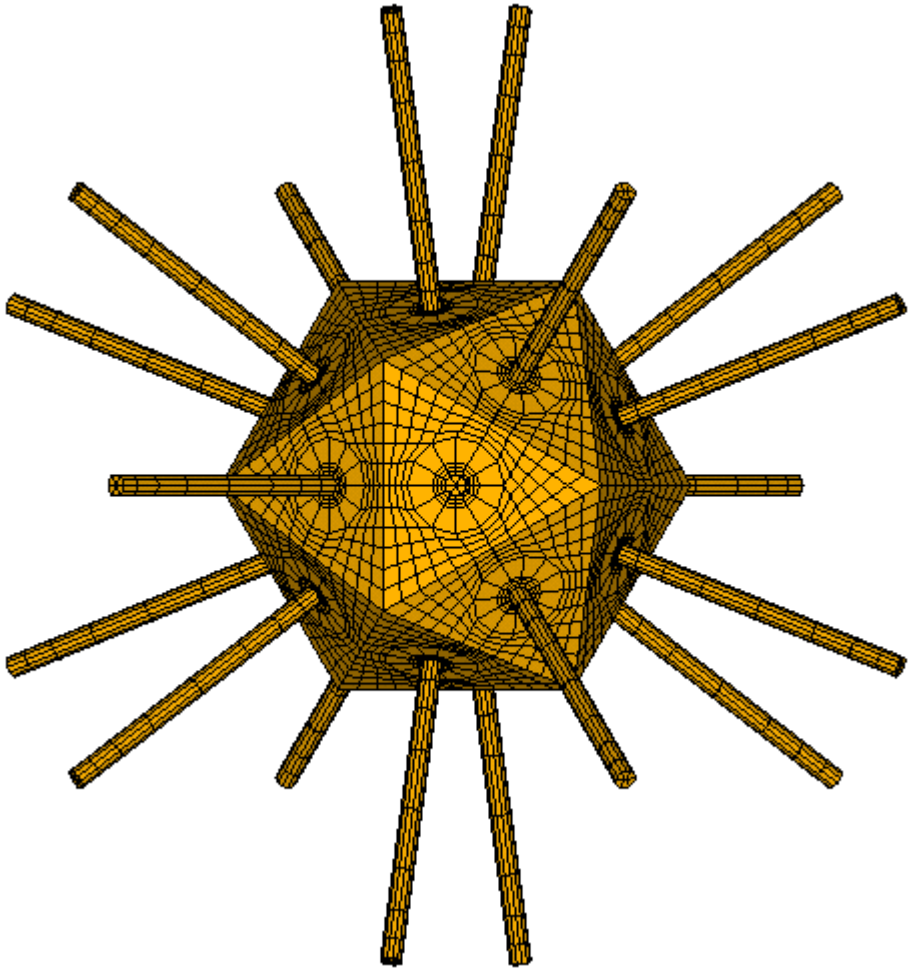

2. CHANNEL MECHANISM SIMULATIONS AND ANALYSES IN WIRELESS COMMUNICATIONS

a) Rigorous Numerical Model of MIMO Wireless Communication Channel

Impedance vs Element Distance (Two-element array)

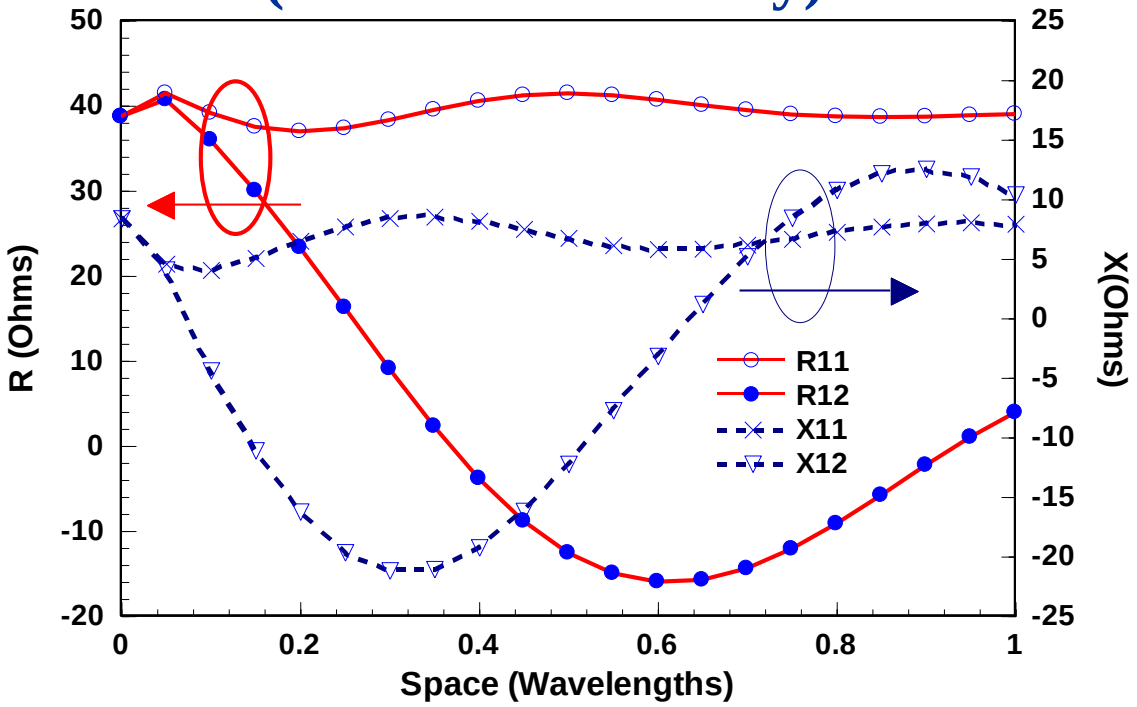

2. CHANNEL MECHANISM SIMULATIONS AND ANALYSES IN WIRELESS COMMUNICATIONS

a) Rigorous Numerical Model of MIMO Wireless Communication Channel

Relation between the input impedance and monopole spacing.

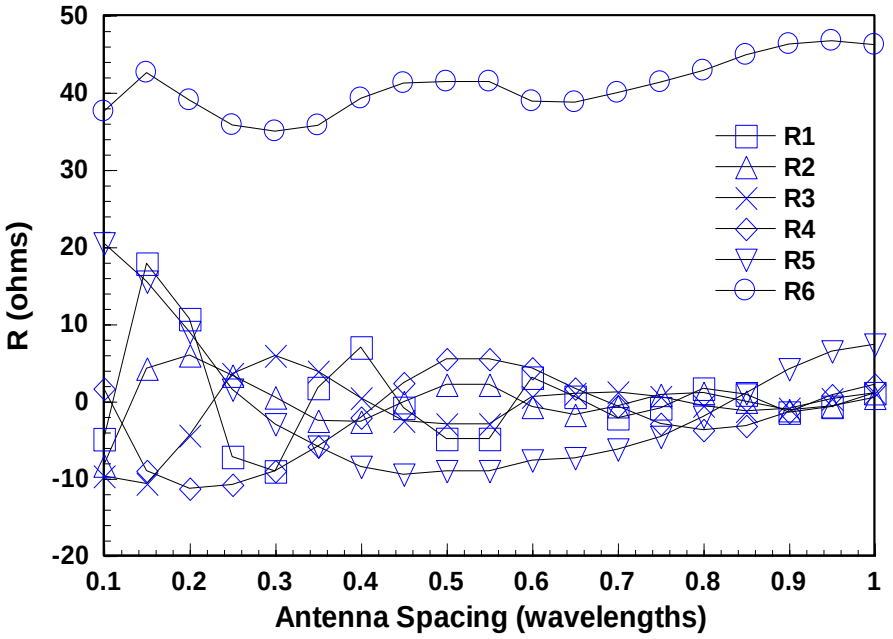

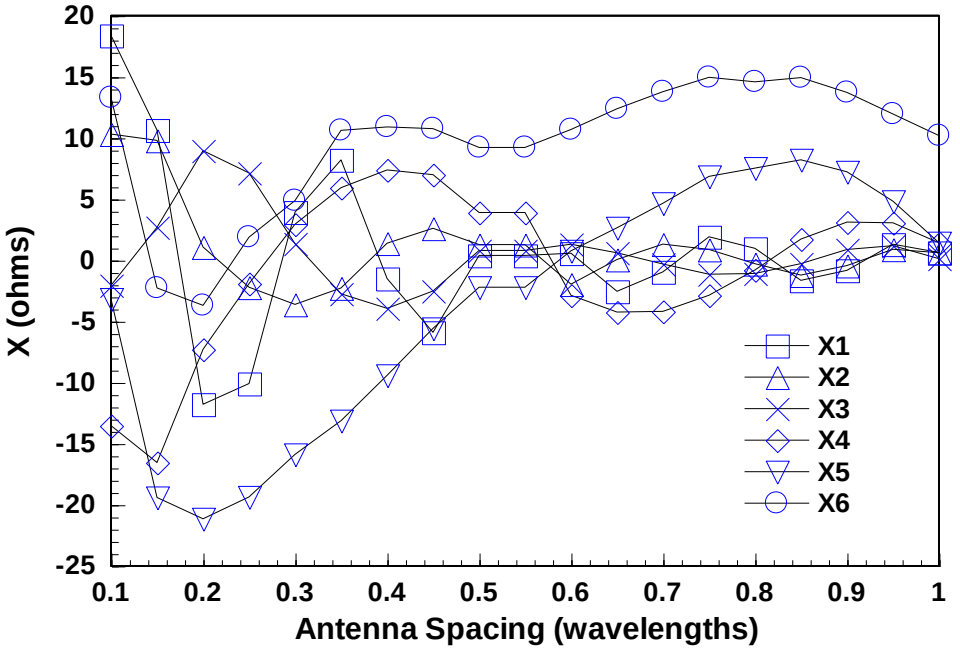

2. CHANNEL MECHANISM SIMULATIONS AND ANALYSES IN WIRELESS COMMUNICATIONS

a) Rigorous Numerical Model of MIMO Wireless Communication Channel

Radiation pattern

One element of the 2-element array:

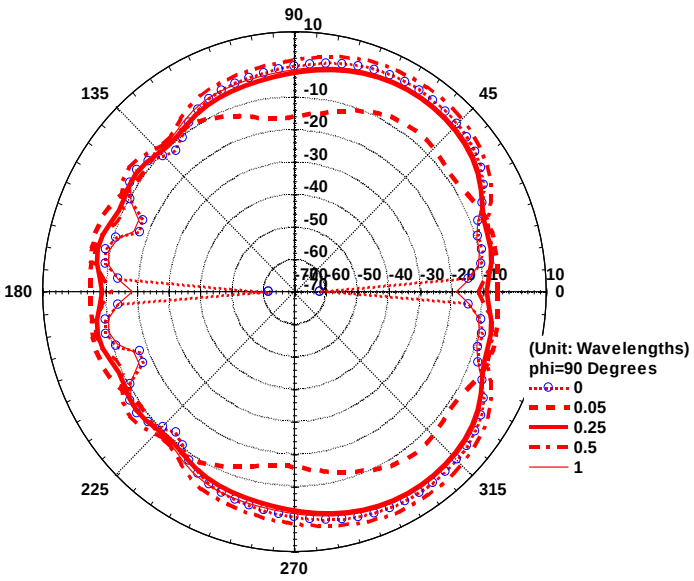

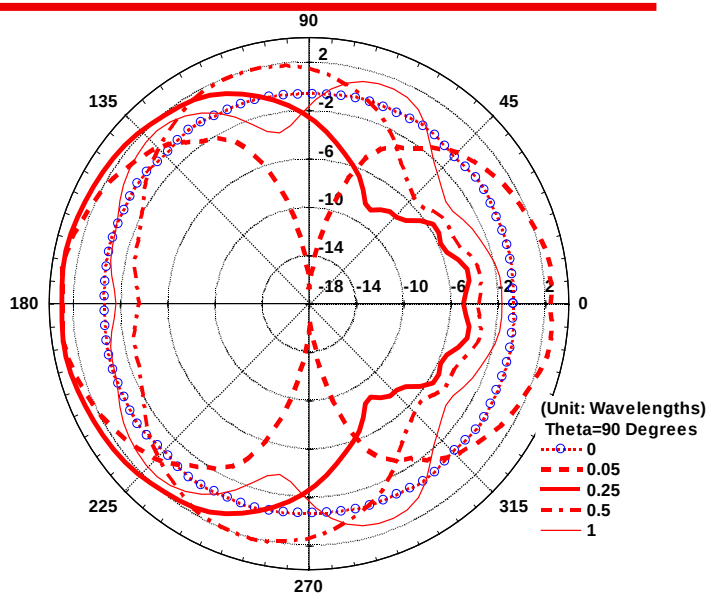

One element of the icosahedron array:

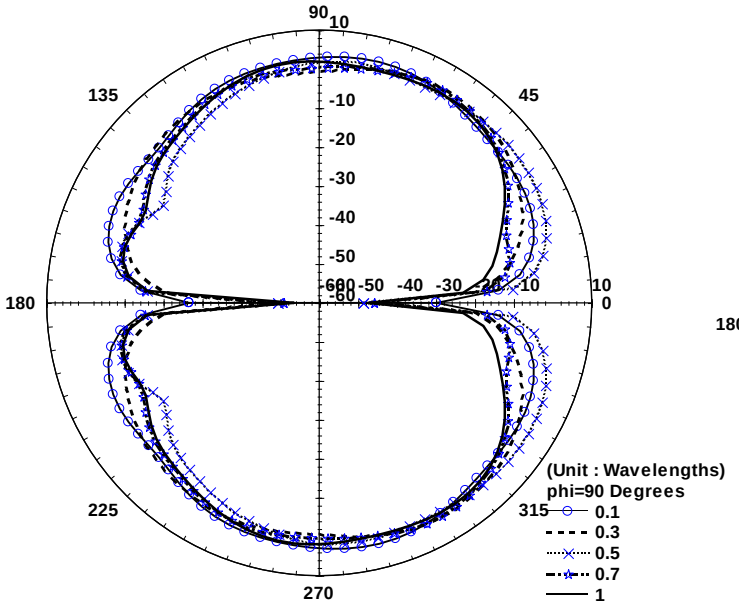

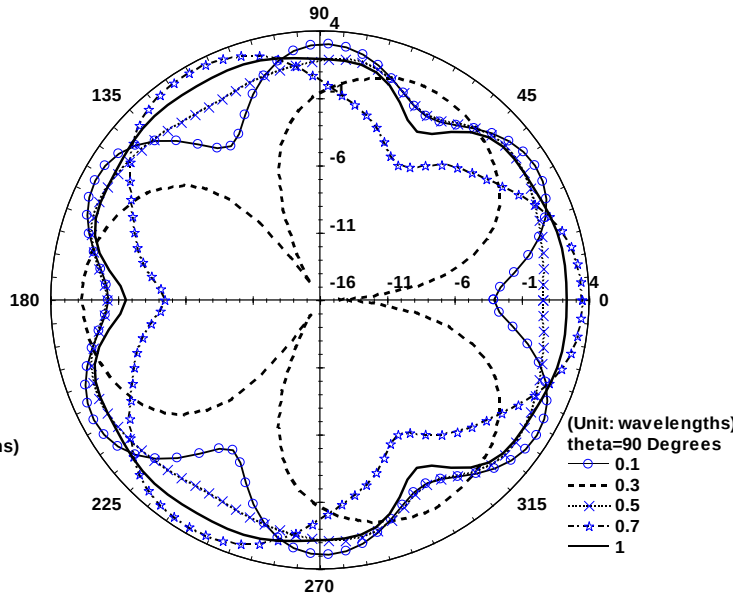

Distribution of the Normalized Channel Matrix Entries

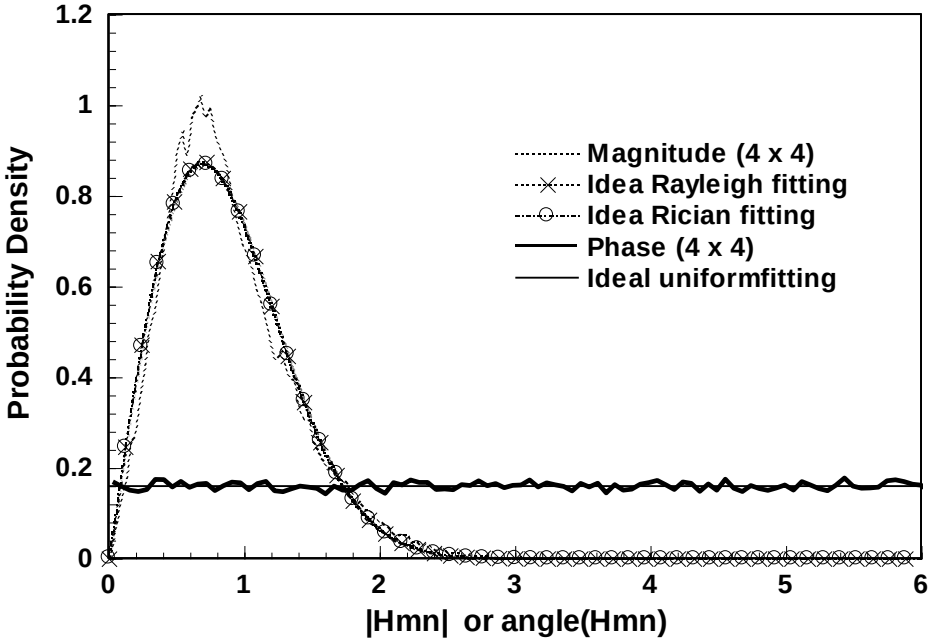

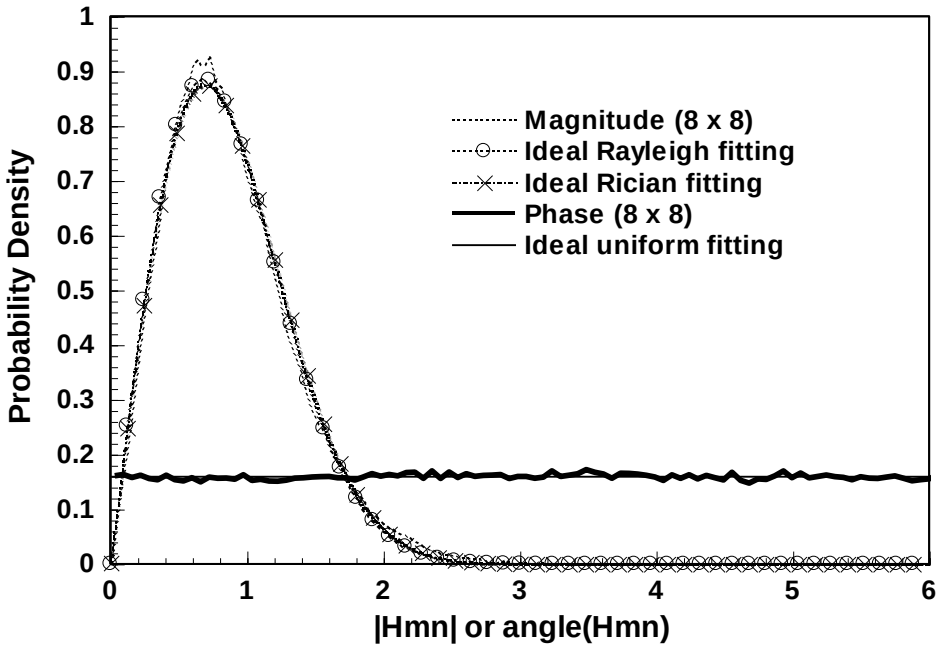

Capacity of the MIMO with Planar Array

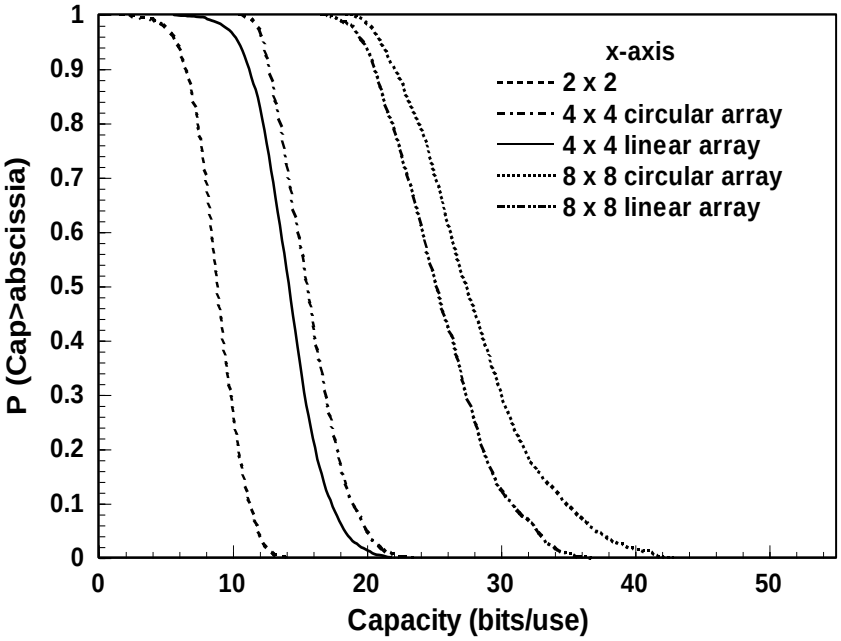

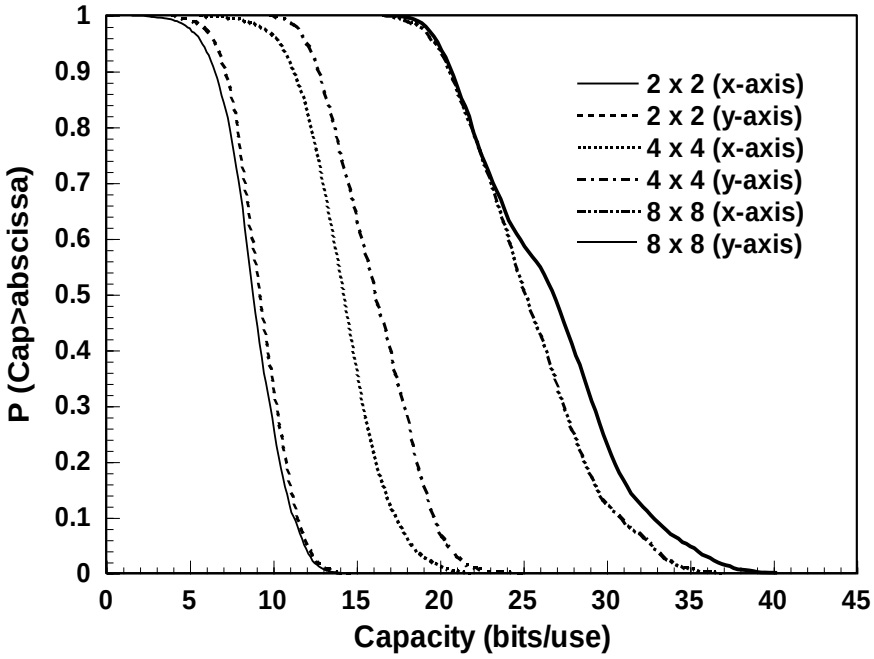

20*20 with Planar arrays vs 20*20 with iosahedron arrays

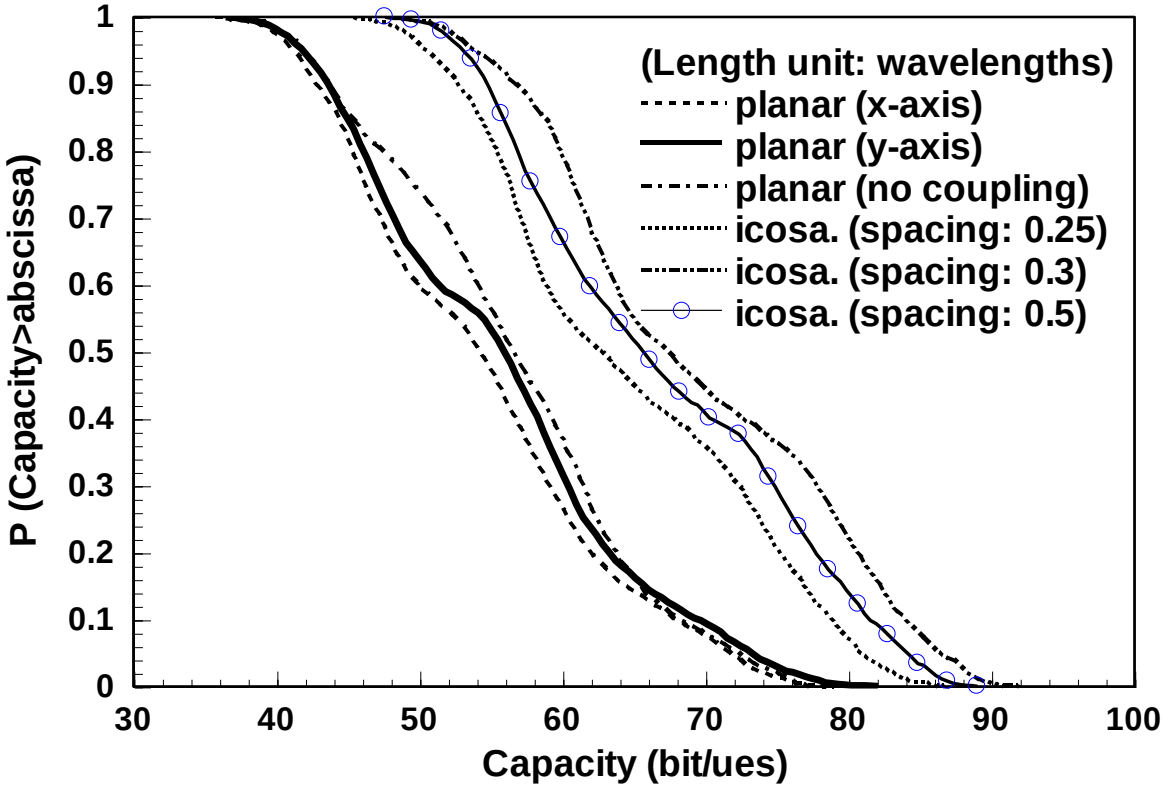

Some terminologies:

- Linear Momentum: $\boldsymbol{p} = \int dv \boldsymbol{S}$
- Poynting's vector: $\boldsymbol{S} = \boldsymbol{E} \times \boldsymbol{H}$
- Angular Momentum: $\mathfrak{J} = \int dv (\boldsymbol{r} \times \boldsymbol{S})$
- In a beam geometry the angular momentum can be decomposed into two parts: $\mathfrak{J} = \boldsymbol{\Sigma} + \boldsymbol{\mathcal{L}}$
- Spin Angular Momentum: $\boldsymbol{\Sigma}$, corresponds to the polarization
- Orbital Angular Momentum: $\boldsymbol{\mathcal{L}}$, corresponds to the phase variations on the plane perpendicular to the beam.

In recent years, researches on OAM in optical domain and in radio frequency (RF) domain, including OAM generation and measurement, attract much attention because of its benefit of increasing spectrum availability and occupancy.

L. Allen, M. W. Beijersbergen, R. J. C. Spreeuw, and J. P. Woerdman, "Orbital angular momentum of light and the transformation of Laguerre-Gaussian laser modes," Phys. Rev. A 45(11), 8185-8189 (1992).

G. Gibson, J. Courtial, M. Padgett, M. Vasnetsov, V. Pas' ko, S. Barnett, and S. Franke-Arnold, "Free-space information transfer using light beams carrying orbital angular momentum," Opt. Express 12(22), 5448-5456 (2004).

B. Thidé, H. Then, J. Sjöholm, K. Palmer, J. Bergman, T. D. Carozzi, Ya. N. Istomin, N. H. Ibragimov, and R. Khamitova, "Utilization of photon orbital angular momentum in the low-frequency radio domain," Phys. Rev. Lett. 99(8), 087701 (2007).

B. Thidé, F. Tamburini, E. Mari, F. Romanato, and C. Barbieri, "Radio beam vorticity and orbital angular momentum," arXiv preprint arXiv:1101.6015 (2011).

How to Generate the OAM?

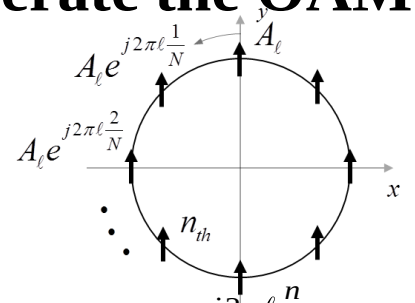

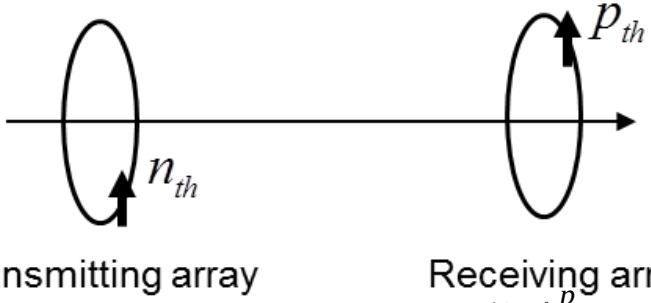

$$s_{\ell n}(t) = A_\ell e^{j2\pi\ell\frac{n}{N}} e^{j2\pi ft}$$

Amplitude Phase Carrier

$$r_{\ell p}(t) = B_\ell e^{j2\pi\ell\frac{p}{N}} e^{j2\pi ft}$$

Amplitude Phase Carrier

Combination of Multiple States

$$s_n = \sum_{\ell=0}^{L-1} A_\ell e^{j2\pi\ell\frac{n}{N}}.$$

$$r_p = \sum_{\ell=0}^{L-1} B_\ell e^{j2\pi\ell\frac{p}{N}}.$$

DFT

$$R_i = \sum_{p=0}^{N-1} r_p e^{-j2\pi i\frac{p}{N}} = \sum_{p=0}^{N-1}\sum_{\ell=0}^{L-1} B_\ell e^{j2\pi\ell\frac{p}{N}} e^{-j2\pi i\frac{p}{N}},$$

$$R_i = \begin{cases} NB_i, & \text{if OAM mode } i \text{ is used} \\ 0, & \text{else} \end{cases}.$$

2. CHANNEL MECHANISM SIMULATIONS AND ANALYSES IN WIRELESS COMMUNICATIONS

b) Orbital Angular Momentum Study.

Enhancement of the Spatial Flexibility in OAM Communications Using Beam Deflections

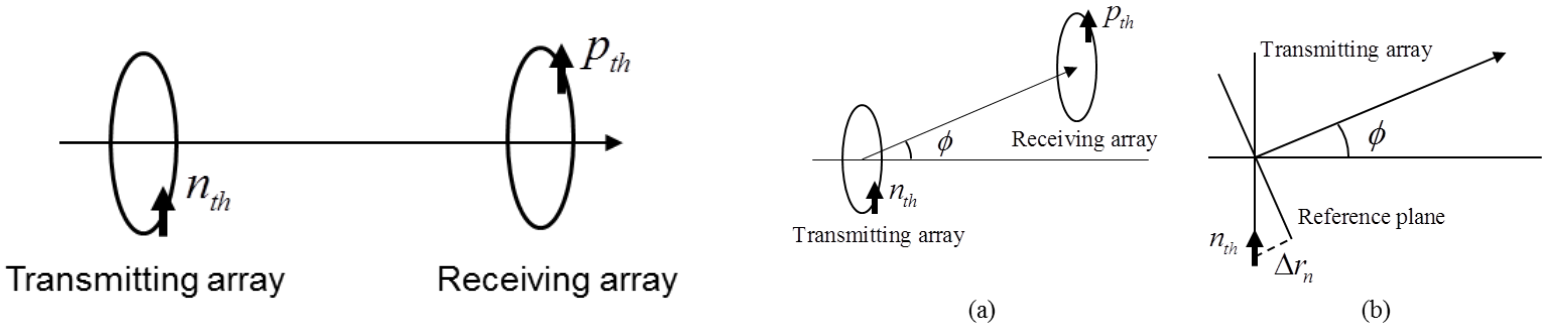

Conventionally, the OAM beam is parallel to the array axis of both the transmitter and the receiver. (See the left.)

In Orbital Angular Momentum (OAM) communications, if the center of the receiving array deviates from the OAM beam generated by the transmitter or the orientation of the receiver is different from that of the OAM beam, the communication quality will degrade drastically. (See the right.)

Deflection of the OAM Beams

Phase correction on the side of the transmitter:

$$\Delta\psi_n = 2\pi\frac{\Delta r_n}{\lambda} = k\Delta r_n.$$

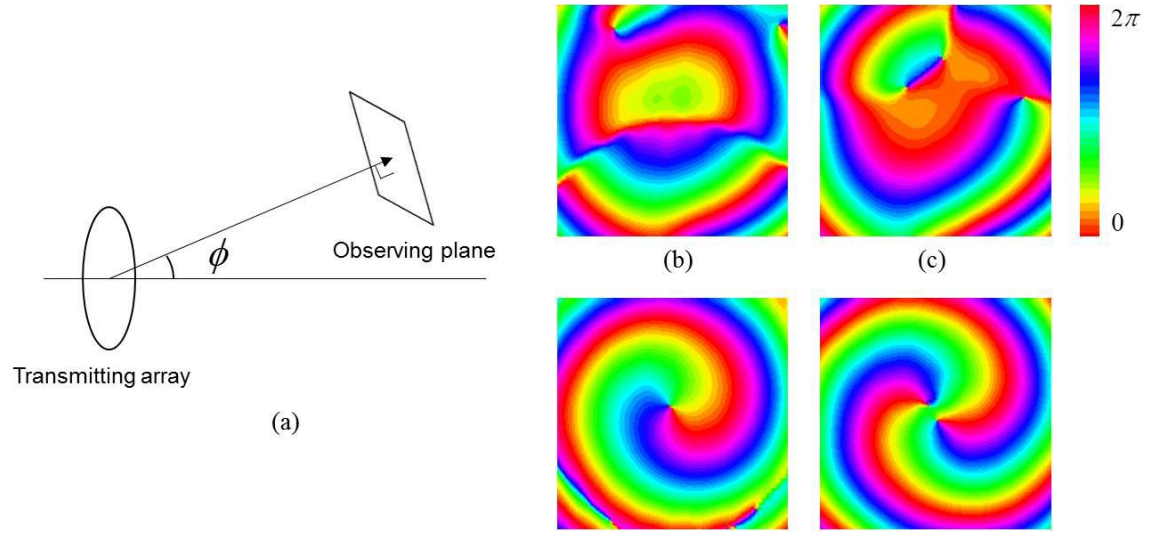

Fig. 5. The position of the observing plane and the phase distribution of different OAM states. (a) The center of the observing plane is 10 wavelengths away from the transmitting array in the perpendicular direction. The array has a radius of 1.5 wavelength. $\phi = 25°$. (b) Phase distribution in the observing plane of OAM state $\ell = 1$ without phase correction. (c) Phase distribution in the observing plane of OAM state $\ell = 2$ without phase correction. (d) Phase distribution in the observing plane of OAM state $\ell = 1$ with phase correction. (e) Phase distribution in the observing plane of OAM state $\ell = 2$ with phase correction.

2. CHANNEL MECHANISM SIMULATIONS AND ANALYSES IN WIRELESS COMMUNICATIONS

b) Orbital Angular Momentum Study.

Demodulation of the Deflected OAM signals

An inverse phase correction is needed on the side of receiver.

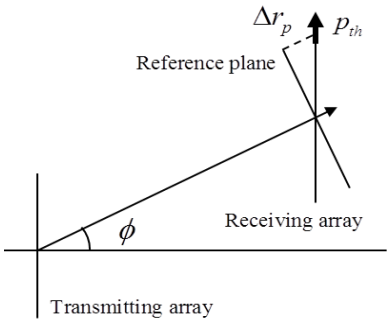

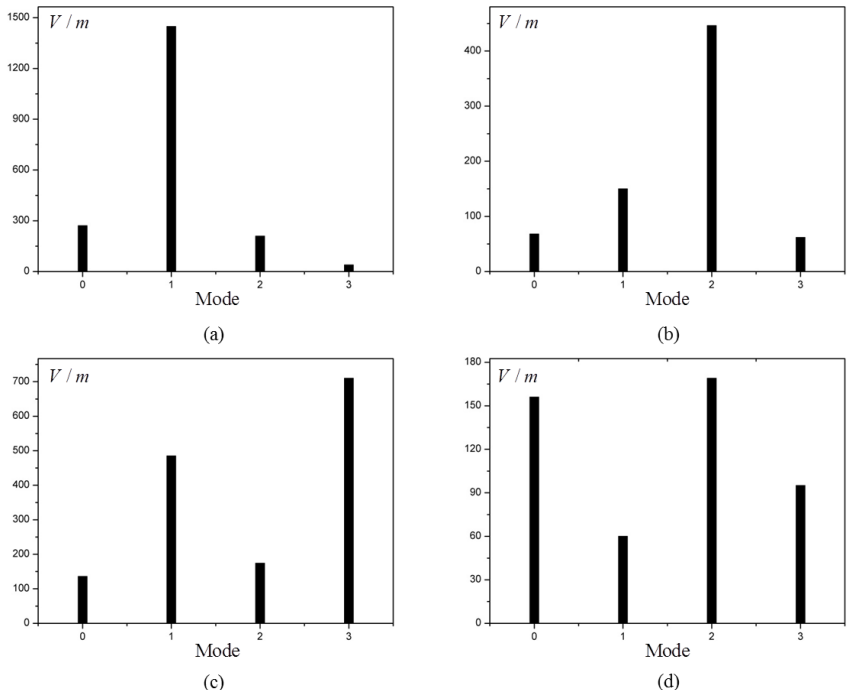

Fig. 8. Demodulation results of deflected OAM beams when modes (a) $\ell = 1$ and (b) $\ell = 2$ are received with phase correction in the receiver, and when modes (c) $\ell = 1$ and (d) $\ell = 2$ are received without phase correction in the receiver.

Huan Yu, Haogang Wang, Xiaofeng Jin, Xianmin Zhang, and Lingfang He, "Enhancement of the Spatial Flexibility in Orbital Angular Momentum Communications Using Beam Deflections," submitted to Optics Express.

2. CHANNEL MECHANISM SIMULATIONS AND ANALYSES IN WIRELESS COMMUNICATIONS

b) Orbital Angular Momentum Study.

Near-field Communications with Orbital Angular Momentum Calculated Using MLGFIM

Near-field channel matrix

$$\overline{\overline{\mathbf{H}}} = [-(\overline{\overline{\mathbf{Z}}}_L^{-1} + \overline{\overline{\mathbf{Y}}}_r) + \overline{\overline{\mathbf{Y}}}_{rt} \cdot (\overline{\overline{\mathbf{Y}}}_t + \overline{\overline{\mathbf{Z}}}_s^{-1}) \cdot \overline{\overline{\mathbf{Y}}}_{tr}]^{-1} \cdot \overline{\overline{\mathbf{Y}}}_{rt} \cdot (\overline{\overline{\mathbf{Z}}}_L^{-1} + \overline{\overline{\mathbf{Y}}}_r)^{-1} \cdot \overline{\overline{\mathbf{Z}}}_s^{-1}$$

Relation between the received signal and the transmitter one:

$$\overline{V}_r = \overline{\overline{\mathbf{H}}} \cdot \overline{V}_s$$

Instead of using ray tracing to calculate the Yrt, here we calculate both Yrt and Ytr using MLGFIM, since both the transmitter and the receiver are very close to each other.

Can we use the far field channel matrix?

$$\overline{\overline{H}} = -(\overline{\overline{Z}}_L^{-1} + \overline{Y}_r)^{-1} \cdot \overline{\overline{Y}}_{rt} \cdot (\overline{\overline{Z}}_s^{-1} + \overline{Y}_t)^{-1} \cdot \overline{\overline{Z}}_s^{-1}$$

2. CHANNEL MECHANISM SIMULATIONS AND ANALYSES IN WIRELESS COMMUNICATIONS

b) Orbital Angular Momentum Study.

Error of the Far Field Channel Matrix Approximation

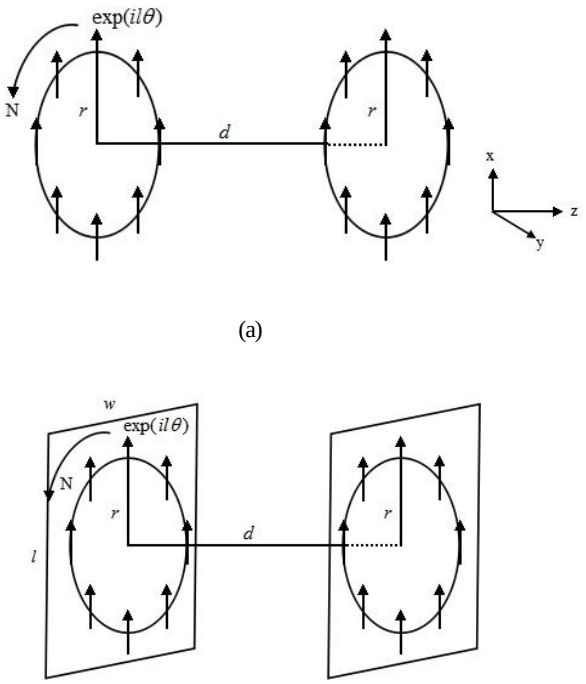

The OAM system composed of dipole arrays as transmitters and receivers. (a) is conventional system without ground, (b) is one with ground.

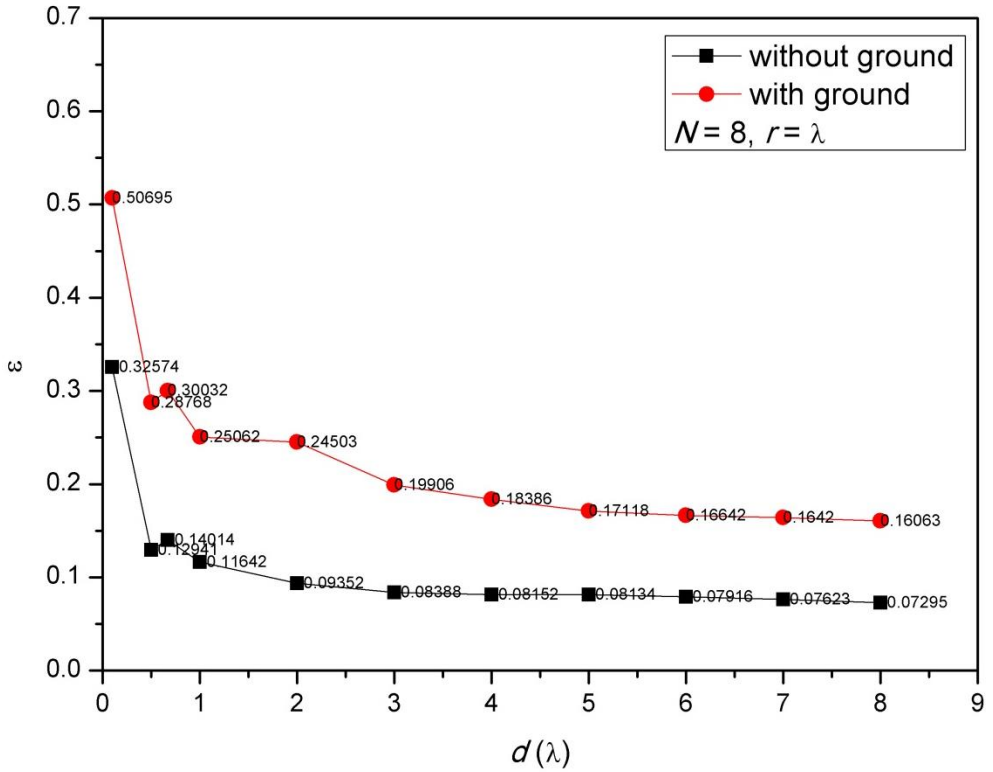

Error of the far field channel matrix versus *the distance d*. Set *N*=8, *r*=λ. The red line is for the case of the OAM system with ground, while the black without ground.

Since the coupling between transmitter and the receiver is very strong, the far field channel matrix approximation is not accurate!

2. CHANNEL MECHANISM SIMULATIONS AND ANALYSES IN WIRELESS COMMUNICATIONS

b) Orbital Angular Momentum Study.

Array with Ground

Demodulated Signal when two modes l=1 and l=2 are excited.

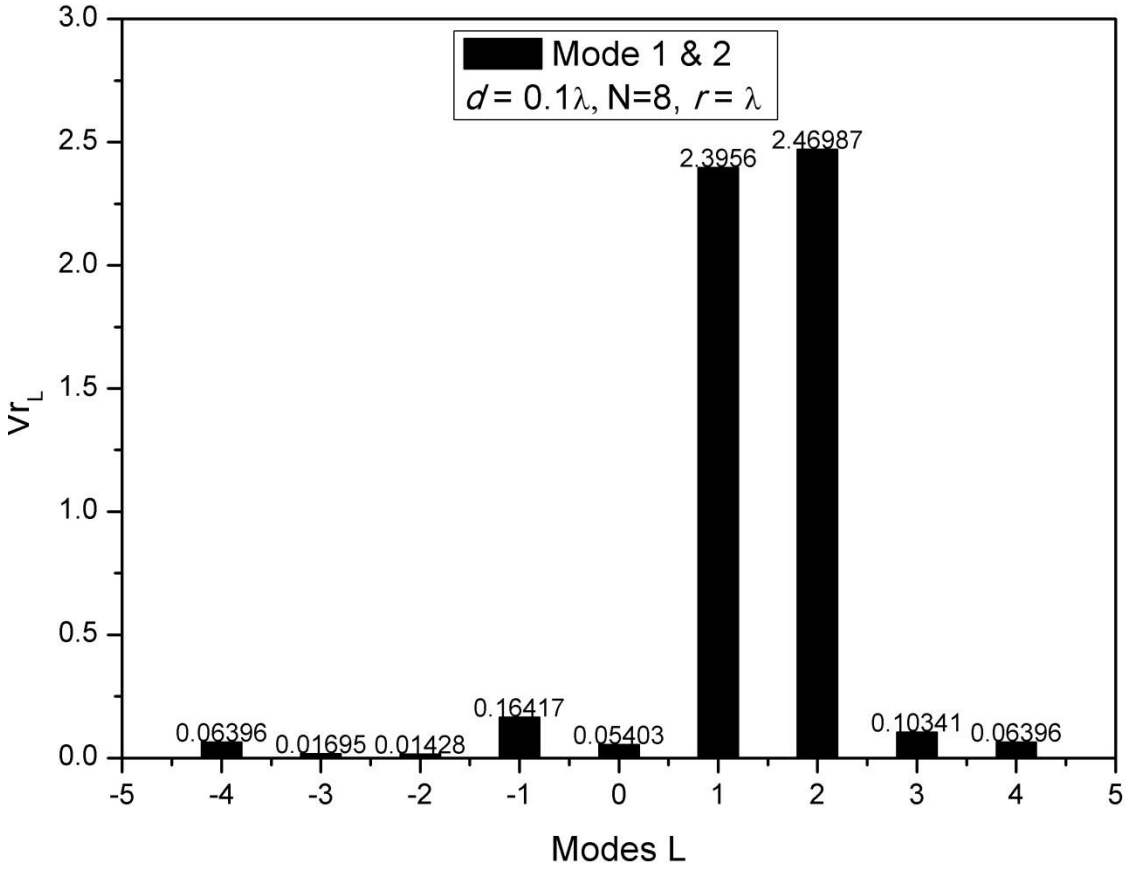

2. CHANNEL MECHANISM SIMULATIONS AND ANALYSES IN WIRELESS COMMUNICATIONS

b) Orbital Angular Momentum Study.

Phase Distribution

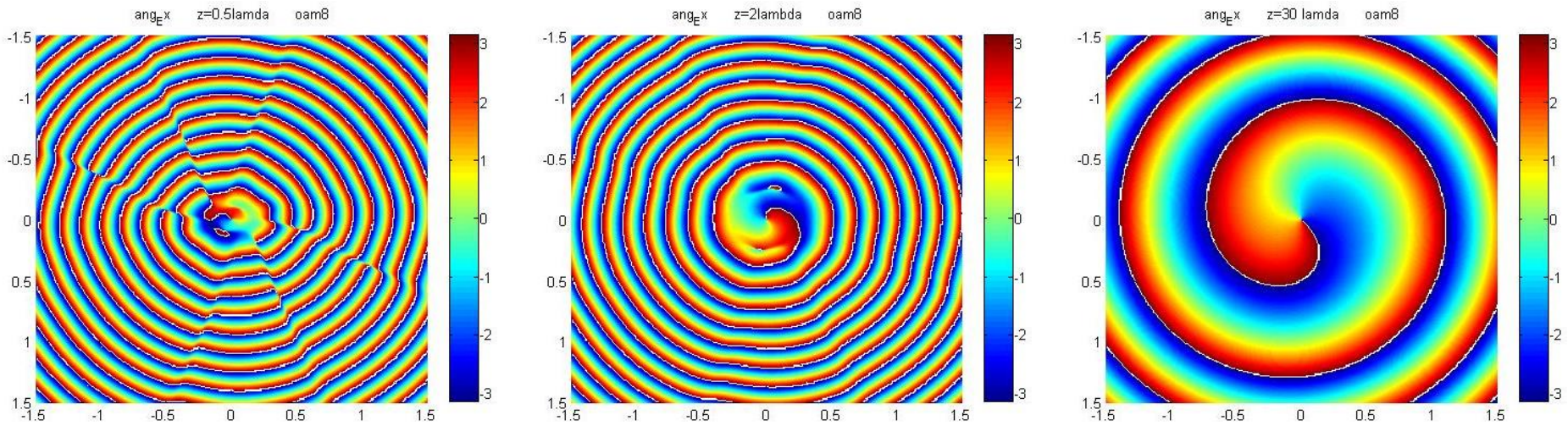

The phase calculated by MLGFIM at the distance of 0.5λ(left) , 2λ(middle) and 30λ(right)

3. SUPERLENS IMAGING

- **Pendry，2000 year, proposed that the films of the noble metals can enhance the higher order modes of the fields, and thus can be used to realize the deep sub-wavelength image. This is the original idea of the superlens.**

- **Xiang Zhang: 2005 experimentally realized the superlens.**

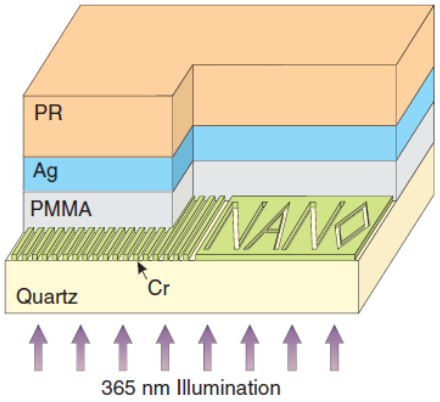

Fig. 1. Optical superlensing experiment. The embedded objects are inscribed onto the 50-nm-thick chrome (Cr); at left is an array of 60-nm-wide slots of 120 nm pitch, separated from the 35-nm-thick silver film by a 40-nm PMMA spacer layer. The image of the object is recorded by the photoresist on the other side of the silver superlens.

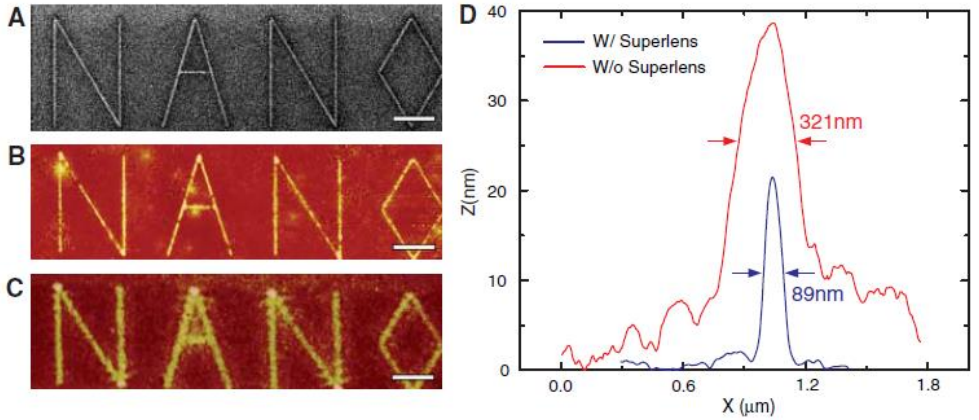

Fig. 4. An arbitrary object "NANO" was imaged by silver superlens. (A) FIB image of the object. The linewidth of the "NANO" object was 40 nm. Scale bar in (A) to (C), 2 μm. (B) AFM of the developed image on photoresist with a silver superlens. (C) AFM of the developed image on photoresist when the 35-nm-thick layer of silver was replaced by PMMA spacer as a control experiment. (D) The averaged cross section of letter "A" shows an exposed line width of 89 nm (blue line), whereas in the control experiment, we measured a diffraction-limited full width at half-maximum line width of 321 ± 10 nm (red line).

- **J. B. Pendry, "Negative refraction makes a perfect lens," Phys. Rev. Lett. 85, 3966-3969 (2000).**
- **N. Fang, H. Lee, C. Sun, and X. Zhang, "Sub-diffraction-limited optical imaging with a silver superlens," Science 308, 534-537 (2005).**

Potential Usage of Superlens

- Integrated Circuits Lithography.
- Biomedical Images.
- The idea of far field superlens has the potential to be used in wireless communctions.

(higher order evanescent modes convert to lower order propagation modes by periodic or non-periodic structures and vice versa.)

3. SUPERLENS IMAGING

The Research Cooperating with University of Washington.

- **Haogang Wang,** J. Q. Bagley, L. Tsang, S. Huang, K.-H. Ding, and A. Ishimaru, “Image enhancement for flat and rough film plasmon superlenses by adding loss,” *J. Opt. Soc. Am. B*, 28, 2499-2509, 2011.

- **Haogang Wang,** Leung Tsang, Shaowu Huang “Loss and back-coupling effects on subwavelengthimaging of three-dimensional superlens,”, OPTICS LETTERS, Vol. 37, No. 12, 2262-2264, June 15, 2012.

Found that

1) when the loss is added in the image region the resolution can be enhanced;

2) the back-coupling can also enhance the resolution.

3. SUPERLENS IMAGING

A superlens structure

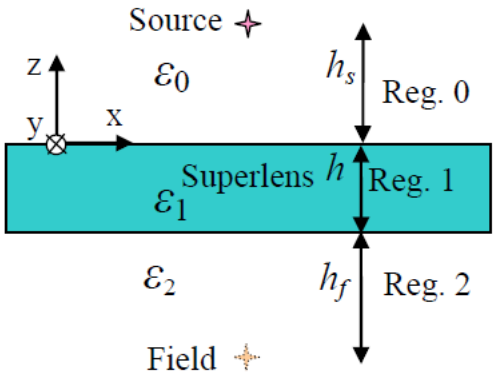

Hy field of 2D Case

$$H_y = \frac{i}{4\pi}\int_{-\infty}^{\infty} dk_x \frac{e^{ik_x x}}{k_{0z}} e^{ik_{0z}z'} T_{02}^{TM} e^{-ik_{2z}z}$$

$$= \frac{i}{4\pi}\int_{-\infty}^{\infty} dk_x \frac{e^{ik_x x}}{k_{0z}} T^{TM}(k_x; z, z')$$

For an ideal superlens, The TM transfer function equals 1.

But this only exists in electrostatic case. However, the superlens operates in optical frequency.

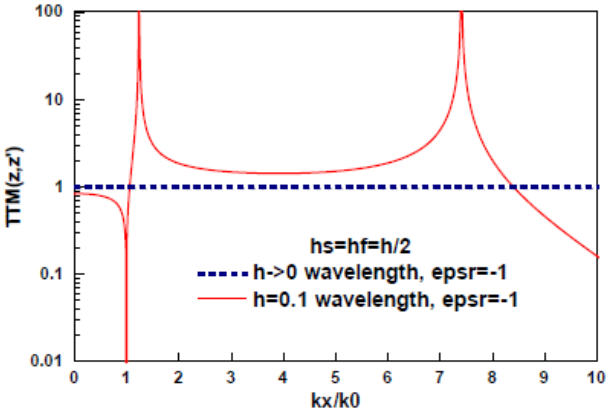

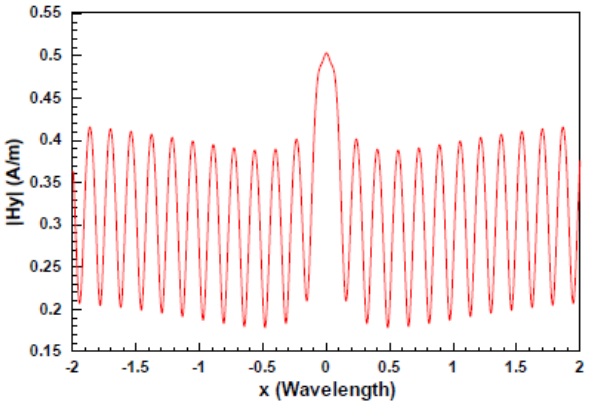

Imaging of the superlens for the case that h=0.1, epsr=-1, and hf=hs=h/2.

3. SUPERLENS IMAGING

- Idea: to add loss in imaging region.

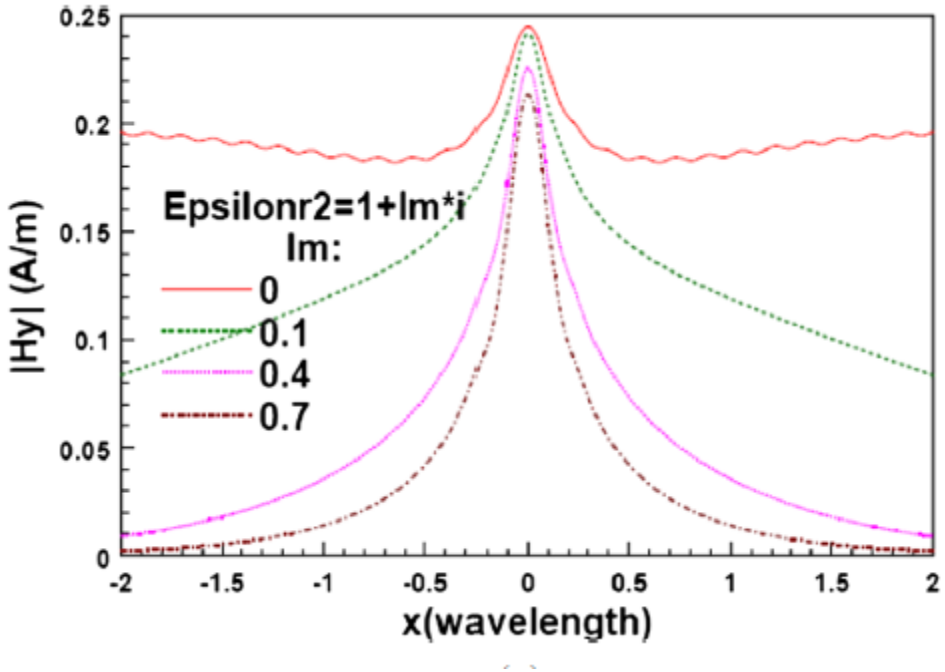

Epsilon1=-1， hf=hs=h=0.1 wavelength

A more realistic 2D case

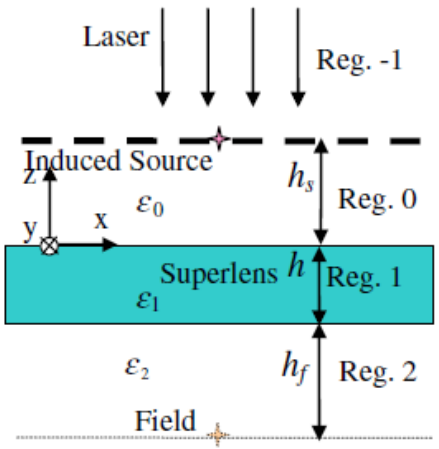

The transfer function takes into account the back coupling of the Chromium mask

$$T_{bc}^{TM}(k_x;z,z') = T^{TM}(k_x;z,z')(1+R_{0,-1}^{TM})[1 - r_{01}^{TM}R_{0,-1}^{TM}e^{2ik_{0z}h_s}]^{-1},$$

Total reflection from the mask.

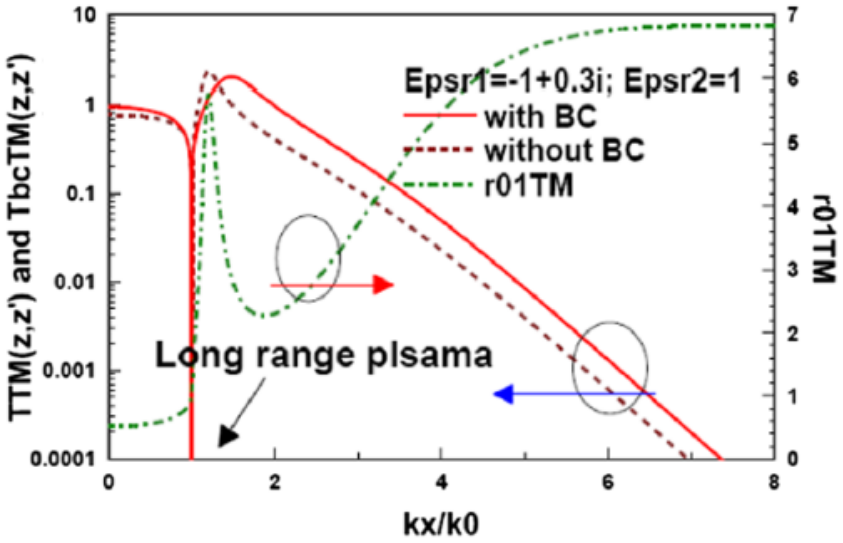

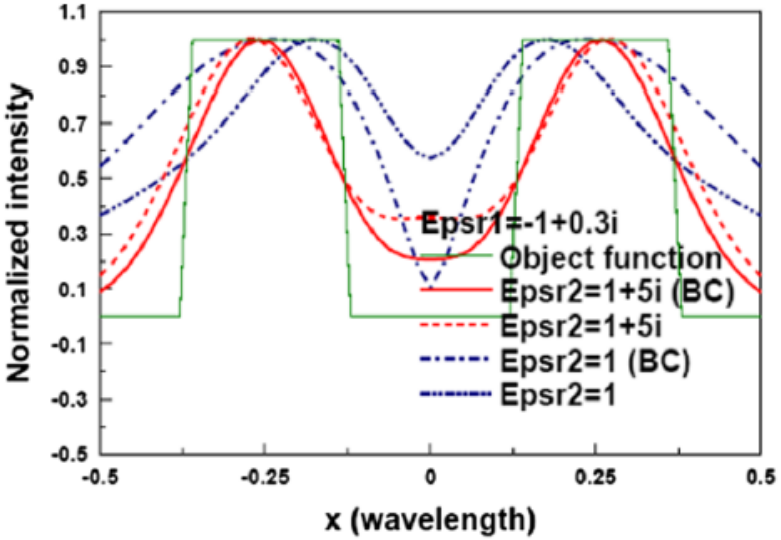

3. SUPERLENS IMAGING

3D cases

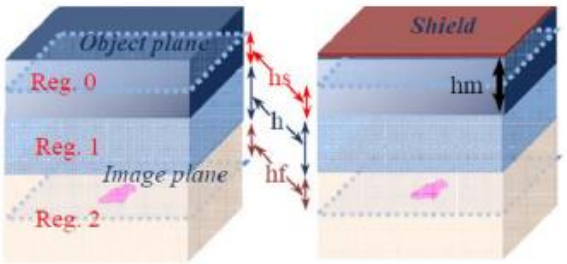

$$\varepsilon_{1r} \approx -1 + 0.3i$$

$$h_s = h_f = 0$$

$$h = 0.1$$

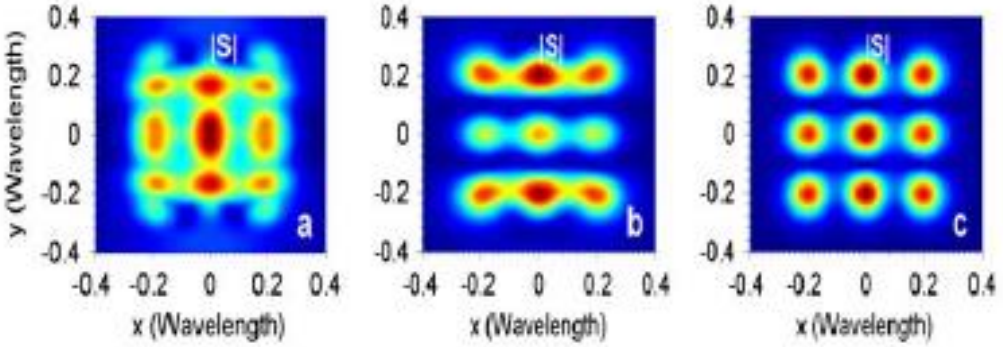

Image of horizontal magnetic dipole array.

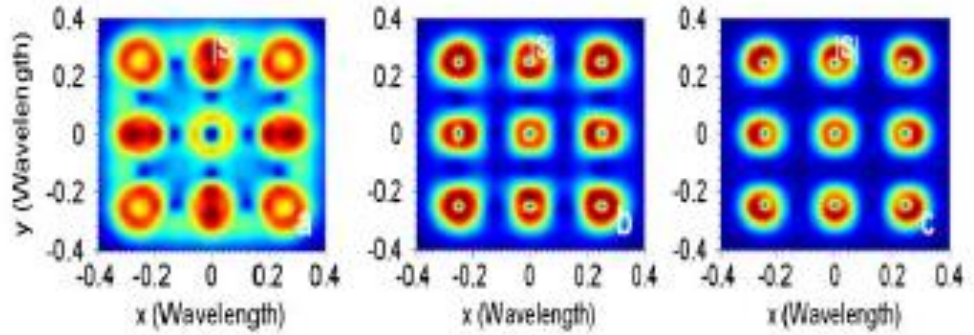

Image of vertical electric dipole array.

Three cases from left to right. w/o loss & w/o b. c., w. loss but w/o b. c., and with both.

Simulation of Lithography

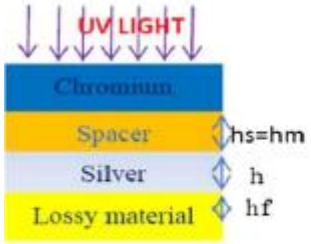

(a)

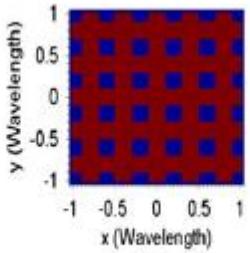

(b)

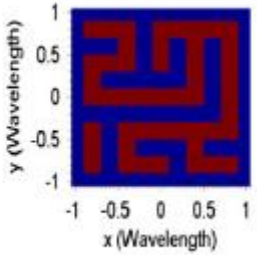

(c)

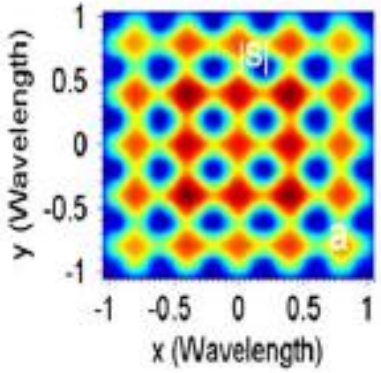

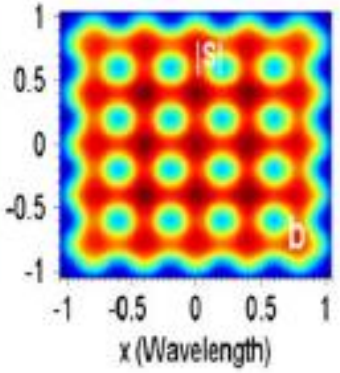

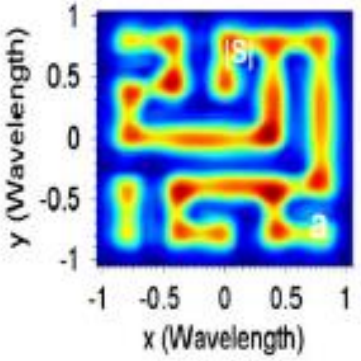

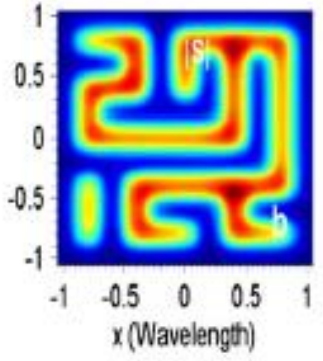

Withno loss **With loss** **Withno loss** **With loss**

$$\varepsilon_{1r} \approx -1 + 0.3i \quad h_s = h_f = 0.01 \quad h = 0.1 \qquad \varepsilon_{2r} = 1 + 1i$$

Thank You for Your Attention!